Development and Application of Efficient Methods for Charge and Exciton Transfer in Organic Semi-conductors

Zur Erlangung des akademischen Grades eines

Doktors der Naturwissenschaften
(Dr. rer. nat.)

von der KIT-Fakultät für Chemie und Biowissenschaften
des Karlsruher Instituts für Technologie (KIT)
genehmigte

Dissertation

von

M. Sc. Farhad Ghalami

Erster Gutachter: Prof. Dr. Marcus Elstner
Zweiter Gutachter: Prof. Dr. Wolfgang Wenzel

Tag der mündlichen Prüfung: 19. Juli 2023

Karlsruhe, 2026

Karlsruhe Institute of Technology
Institute of Physical Chemistry
Fritz-Haber-Weg 2
76131 Karlsruhe

Abstract

This thesis we tried to investigate some challenges in the field of organic semi-conductors (OSCs) regarding the charge and energy transfer phenomena using efficient computational models. Therefor, this thesis contains 5 chapters. In chapter 1, we provide an introduction to organic semi-conductors (OSCs). In the second chapter, we briefly discuss the basics of theoretical methods used in this research. In chapter 3 we provide a fundamental background describing the mechanism of charge transport in pentacene based SurMOF structure. Our theoretical findings have confirmed that the transport mechanism along the 1D PEN stacks is primarily influenced by dynamic contributions. These contributions arise from the rotations of the PEN linkers around the 6,13-axis, which is defined by the two metal-coordinating carboxylate groups. The frustrated rotation leads to fluctuations in the inter-PEN electronic coupling and dynamic disorder. As a result, there is partial delocalization of holes and a charge transport mechanism that lies at the borderline between localized hopping and delocalized charge transport. By conducting detailed static and dynamic quantum-mechanical investigations, we have gained insights into the fundamental principles that govern the charge carrier properties of such arrays of OSC compounds.

In chapter 4, we tried to establish a method to deeply investigate specific phonon modes responsible for the deterioration of the charge mobility in OSCs (killer modes). We examined the effect of this specific collective motions on the hole mobility of the anthracene as our test case using the fewest switches surface hopping algorithm to propagate the charge through the material.

Finally, in chapter 5, we present a multiscale method for the propagation of Frenkel singlet exciton in OSCs using neural network models that predict site energies and excitonic couplings together with their derivatives which are critical for our non-adiabatic molecular dynamics calculation scheme. We used the fewest switches surface hopping algorithm (FSSH) to propagate the exciton through our systems. Long-range correction version of density functional tight-bonding with self consistence charges (LC-DFTB2) has been used

to generate high-quality data required for the networks to be trained. In this work we considered for types of OSCs crystals, Anthracene (ANT), Pentacene (PEN), Perylenediimide (PDI), and Diindenoperylene (DIP) to calculate their exciton diffusion constant using the abovementioned method.

Zusammenfassung

In dieser Arbeit haben wir versucht, einige Herausforderungen im Bereich der organischen Halbleiter (OSCs) im Hinblick auf die Ladungs- und Energietransferphänomene mithilfe effizienter Rechenmodelle zu untersuchen. Aus diesem Grund umfasst diese Arbeit 5 Kapitel. Im ersten Kapitel geben wir eine Einführung in organische Halbleiter (OSCs). Im zweiten Kapitel erläutern wir kurz die Grundlagen der theoretischen Methoden, die in dieser Forschung verwendet wurden.

Im dritten Kapitel bieten wir einen grundlegenden Hintergrund, der den Mechanismus des Ladungstransports in einer pentacenbasierten SurMOF-Struktur beschreibt. Unsere theoretischen Ergebnisse haben bestätigt, dass der Transportmechanismus entlang der 1D PEN-Stapeln hauptsächlich von dynamischen Beiträgen beeinflusst wird. Diese Beiträge entstehen aus den Rotationen der PEN-Verbindungen um die 6,13-Achse, die durch die beiden metallkoordinierenden Carboxylatgruppen definiert ist. Die frustrierte Rotation führt zu Schwankungen in der inter-PEN-elektronischen Kopplung und zu dynamischer Unordnung. Dadurch kommt es zu einer teilweisen Delokalisierung von Löchern und einem Ladungstransportmechanismus, der an der Grenze zwischen lokalisiertem Hopping und delokalisiertem Ladungstransport liegt. Durch detaillierte statische und dynamische quantenmechanische Untersuchungen haben wir Einblicke in die grundlegenden Prinzipien gewonnen, die die Ladungsträgereigenschaften solcher OSC-Verbindungen beeinflussen.

Im vierten Kapitel haben wir versucht, eine Methode zur eingehenden Untersuchung spezifischer Phononmoden zu etablieren, die für die Verschlechterung der Ladungsbeweglichkeit in OSCs verantwortlich sind (sogenannte "Killer-Moden"). Wir haben den Einfluss dieser spezifischen kollektiven Bewegungen auf die Ladungsbeweglichkeit von Anthracen als Fallbeispiel untersucht, wobei wir den Fewest-Switches-Surface-Hopping-Algorithmus verwendet haben, um die Ladung durch das Material zu propagieren.

Schließlich präsentieren wir in Kapitel 5 eine multiskalige Methode zur Propagation von Frenkel-Singulett-Exzitonen in OSCs unter Verwendung neuronaler Netzwerkmodelle, die Site-Energien und exzitonische Kopplungen zusammen mit ihren Ableitungen vorhersagen, die für unser nichtadiabatisches Molekulardynamik-Berechnungsschema entscheidend sind. Wir haben den Fewest-Switches-Surface-Hopping-Algorithmus (FSSH) verwendet, um die Exzitonen durch unsere Systeme zu propagieren. Für die Schulung der Netzwerke wurde die LC-DFTB2-Methode (Long-Range-Corrected Density Functional Tight-Binding) mit selbstkonsistenten Ladungen verwendet, um hochwertige Daten zu generieren. In dieser Arbeit haben wir vier Arten von OSC-Kristallen betrachtet: Anthracene (ANT), Pentacen (PEN), Perylenediimide (PDI), und Diindenoperylene (DIP), um ihre Exzitonen-Diffusionskonstante mithilfe

Acknowledgements

First and foremost, I would like to express my special appreciation and thanks to my advisor, Prof. Marcus Elstner. I am profoundly grateful for his unwavering support throughout the past three years. His patience and understanding during the challenging times of my Ph.D. journey have been invaluable. Moreover, his relentless drive to push me to become a better researcher and person has had a significant impact on my growth.

I would also like to extend my heartfelt gratitude to Dr. Weiwei Xie, who has been an exceptional mentor, a reliable source of support, and my go-to person whenever I faced challenges during my Ph.D. Weiwei always made himself available for help and provided invaluable advice. I have gained profound insights from every interaction with him during my Ph.D. journey.

Furthermore, I would like to thank all of my collaborators for their contributions and fruitful collaborations. Their expertise and perspectives have enriched my research experience.

I would like to express my sincere thanks to my committee members for their invaluable insights and thought-provoking questions. I am grateful for their dedication to serving on my Ph.D. committee.

A special thanks go to my colleagues and all my friends at KIT. Your friendship, engaging conversations, and shared experiences have created some of the best memories of my Ph.D. years.

Lastly, I would like to express my deepest gratitude to my wife and family for their unwavering support and unconditional love throughout the ups and downs of my Ph.D. journey. Their constant encouragement and belief in me have been the driving force behind my accomplishments.

Contents

Abstract i

Zusammenfassung iii

Acknowledgements v

List of Figures xi

List of Tables xv

1. Introduction 1
1.1. Organic Semi-conductors (OSCs) 1

2. Theoretical Background 5
2.1. Electronic Structure Theory 5
2.1.1. Schrödinger Equation 6
2.1.2. Hamiltonian 6
2.1.3. Born-Oppenheimer Approximation 8
2.1.4. Density Functional Theory 9
2.1.5. Density Functional Tight Binding Method 11
2.2. Molecular Dynamics Simulation 14
2.2.1. Integration Algorithms 14
2.2.2. Thermostats and Barostats 15
2.2.3. Periodic Boundary Conditions 16
2.2.4. Force Fields 16
2.3. Quantum Mechanics/Molecular Mechanics (QM/MM) 19
2.3.1. Fragment Orbital Approximation 19
2.4. Non-adiabatic Molecular Dynamics 20
2.5. Charge and Exciton Transfer 24
2.5.1. Charge Transfer Regimes 24
2.5.2. Exciton Transfer 28

2.6. Machine Learning 29
2.6.1. Artificial Neural Networks 30

3. Charge Transfer in Surface-functionalized Metal Organic Frameworks 33
3.1. Introduction 33
3.2. Methodology 35
3.2.1. System Preparation 35
3.2.2. Mean Squared displacement (MSD) and Hole Mobility 37
3.3. Results and Discussions 37
3.3.1. Charge Transfer 37
3.3.2. Hole Coupling Fluctuations 38
3.3.3. Temperature Dependency of the Hole Mobility . . . 40
3.4. Conclusions 41

4. Charge Phonon Interaction 43
4.1. Introduction 43
4.2. Methodology 44
4.2.1. System Preparation 44
4.2.2. Calculation of the Eigenmotions 44
4.2.3. Principal Component Analysis 45
4.2.4. Mode Elimination 46
4.2.5. Charge Mobility Calculations 46
4.3. Results and Discussion 47
4.3.1. Eigenmodes of the anthracene dimer 47
4.3.2. Killer Mode Identification 47
4.3.3. The Effect of Killer Mode Elimination on the Hole Coupling 50
4.3.4. The Effect of Killer Mode Elimination on the Hole Mobility 50
4.4. Conclusions 52

5. Exciton Transfer using Machine Learned Hamiltonian 53
5.1. Introduction 53
5.2. Methodology 54
5.2.1. Frenkel Exciton 54
5.2.2. Exciton coupling 55
5.2.3. Exciton Reorganization Energy 57
5.2.4. Neural Networks (NN) 58
5.2.5. System Preparation 59

5.3. Results and Discussion 61
5.3.1. Site Energy 61
5.3.2. Exciton Coupling 64
5.3.3. Internal Exciton Relaxation 65
5.3.4. Training Data 67
5.3.5. Neural Network Fitting 69
5.3.6. Exciton Propagation and neural network model validation 72
5.3.7. Exciton Propagation using Trajectory Surface Hopping 74
5.4. Conclusions 77

6. Summary and Outlook **79**

Bibliography **81**

A. Appendix **91**

List of Figures

2.1. Periodic boundary conditions (PBC) in 2D: The central box is replicated in all directions. As soon as a particle cross the PBC in any direction, its replica would replace it. 16

3.1. Supercell of a) Zn-PEN and b) PEN 36
3.2. Superposition of the PEN dimers in Zn-PEN (a) and PEN crystal (b) sampled during QM/MM molecular dynamics simulations at 300 K 39
3.3. The electronic coupling between PEN molecules in the PEN crystal (in blue) and in Zn-PEN (in black) at 300 K. 40
3.4. Temperature dependence of the hole mobility in the Zn-PEN obtained using the direct propagation approach. 41

4.1. Anthracene crystal structure 44
4.2. Eigenvalues of the corresponding eigenmodes of the anthracene dimer in the b direction of the crystal, calculated from the diagonalization of the covariance matrix. 48
4.3. Scanning the hole coupling as a function of displacement along the first six eigenmodes of anthracene dimers in b direction. 1 and -1 correspond to maximum and minimum displacements. . . 49
4.4. Illustration of the first and third eigenmode of ANT dimer in b direction 49
4.5. Projections of eigenvectors, extracted from two different dimers in the simulation box, on each other 51

5.1. Schematic of the reorganization energy (relaxation energy) in the singlet excitonic system. S_0 and S_1 represent the ground and first excited PES of the system. 58
5.2. Illustration of the of a) ANT, b) PEN, c) PDI, and d) DIP crystals. 60

5.3. Comparison of the vertical excitation energy of S_1 [eV] calculated by TD-LC-DFTB2 and TD-DFT using long range separated functionals ωB97xd and CAM-B3LYP with 6-31G(p, d) level of theory. 63
5.4. Comparison of the oscillator strength of S_1 calculated by TD-LC-DFTB2 and TD-DFT using long range separated functionals ωB97xd and CAM-B3LYP with 6-31G(p, d) level of theory. 63
5.5. Coulomb coupling correlation plots of the ANT, PEN, PDI, and DIP. The unit of the coupling values are eV 65
5.6. Locally excited contribution of the excitonic coupling calculated via diabatization technique using TD-LC-DFTB2 for ANT, PEN, PDI, and DIP. 66
5.7. Distribution of the site energy training data of the ANT. PEN, PDI, and DIP 67
5.8. Total exciton coupling vs. Coulomb coupling (Ccpl) for ANT, PEN, PDI, and DIP during a course of MD simulation for 1 ns. . 68
5.9. TrMullCpl vs. Ccpl distribution for the MD sampled structures of the ANT, PEN, PDI, and DIP, calculated by TD-LC-DFTB2. . . 69
5.10. Distribution of the TrMull coupling training data of the ANT. PEN, PDI, and DIP 70
5.11. Coulomb coupling calculated by TD-LC-DFTB2 vs. intermolecular distance. 73

A.1. ANT site energies and reorganization energy distributions, predicted by NN during the NAMD simulation 91
A.2. ANT adir TrMull coupling distribution, predicted by NN during the NAMD simulation 91
A.3. ANT bdir TrMull coupling distribution, predicted by NN during the NAMD simulation 92
A.4. PEN site energies and reorganization energy distributions, predicted by NN during the NAMD simulation 92
A.5. PEN pdir TrMull coupling distribution, predicted by NN during the NAMD simulation 92
A.6. PEN t1dir TrMull coupling distribution, predicted by NN during the NAMD simulation 93
A.7. PEN t2dir TrMull coupling distribution, predicted by NN during the NAMD simulation 93
A.8. PDI site energies and reorganization energy distributions, predicted by NN during the NAMD simulation 93

A.9. PDI pdir TrMull coupling distribution, predicted by NN during the NAMD simulation 94
A.10. PDI t1dir TrMull coupling distribution, predicted by NN during the NAMD simulation 94
A.11. PDI t2dir TrMull coupling distribution, predicted by NN during the NAMD simulation 94
A.12. PDI t3dir TrMull coupling distribution, predicted by NN during the NAMD simulation 95
A.13. ANT MSD adir calculated from NAMD simulation 95
A.14. ANT MSD bdir calculated from NAMD simulation 96
A.15. PEN MSD pdir calculated from NAMD simulation 96
A.16. PEN MSD t1dir calculated from NAMD simulation 97
A.17. PEN MSD t2dir calculated from NAMD simulation 97
A.18. PDI MSD t1dir calculated from NAMD simulation 98

List of Tables

3.1. Transport parameters of the Zn-PEN and PEN crystal. The value of the hole coupling and the reorganization energy is in [meV] and mobility is represented in $cm^2V^{-1}s^{-1}$ 38

4.1. Average and standard deviation of the hole coupling of an anthracene dimer in the b direction before and after eigenmode (E.M.) elimination. The first row shows the restrained eigenmode. 50
4.2. NAMD simulation results of the hole propagation in anthracene b direction under the condition where some eigenmodes of motion are restrained. μ is the hole mobility and IPR is the inverse participation ratio which shows the degree of the charge delocalization 52

5.1. Comparison of the vertical excitation energy [eV] and oscillator strength calculated by TD-LC-DFTB2 and TD-DFT using long range separated functionals ωB97xd and CAM-B3LYP with 6-31G(p, d) level of theory. σ is the relative error of the vertical transition energy calculated by TD-LC-DFTB2 with respect to its value calculated by ωB97xd in [eV]. 62
5.2. Reorganization energy [meV] calculated from LC-DFTB2 and DFT using range separated fuctionals with 6-31G(p, d) level of theory, σ is the value of the relative error. 66
5.3. Neural network models for the TrMull coupling together with the gradients in x, y, and z direction of ANT, PEN, PDI, and DIP in different crystallographic directions. MEA mad Max err. are in [eV]. 71
5.4. Neural network models for the site energies together with the gradients in x, y, and z direction of ANT, PEN, PDI, and DIP. MEA mad Max err. are in [eV]. 72
5.5. short 72

5.6. Exciton coupling and reorganization energy [meV] of ANT, PEN, PDI, and DIP in different crystallographic directions. ⟨⟩ indicates the average values of the properties during a course of MD simulation. 74
5.7. Diffusion constant in $cm^2/s \times 10^{-3}$ and IPR value for the ANT, PEN, PDI, and DIP in different crystallographic directions 76

1. Introduction

1.1. Organic Semi-conductors (OSCs)

Organic semiconductors (OSCs) are a class of materials that exhibit both organic (carbon-based) and semiconductor properties. They have become an important component of electronic devices in recent years, including organic light-emitting diodes (OLEDs) [1–3], organic solar cells [4–6], and organic field-effect transistors (OFETs) [7–9]. OSCs have the advantage of being flexible, lightweight, and easily processed from solution, which makes them attractive for use in applications where traditional inorganic semiconductors are not suitable, and also makes it possible to fabricate large-area devices at low cost with relatively simple processing techniques [10]. However, the exploration of novel OSC candidates with specific properties or the optimization of existing materials can be a costly endeavor due to the vast range of possible compounds. In this context, theoretical approaches employing simulation techniques play a pivotal role by complementing or expediting experimental studies, facilitating efficient screening of a vast chemical space for compounds with promising properties prior to their synthesis. To achieve this, it is imperative to develop fast and robust methods capable of simulating charge and exciton transfer in large molecular systems, while accurately reproducing experimentally observable quantities such as exciton diffusion constant.

Various factors influence the performance of organic electronic devices, including charge carrier mobility and trap density. In comparison to inorganic semiconductors, organic semiconductors typically exhibit lower charge carrier mobility due to the disordered structure of organic materials. Several aspects, such as molecular packing, defects, and the level of disorder in the material, impact charge carrier mobility. The existence of traps in organic semiconductors can impede the movement of charge carriers by capturing

them. These traps may arise from defects within the material itself or impurities introduced during the fabrication process [11].

While the band theory has been successfully used for inorganic semiconductors, it breaks down in OSCs where the mean free path of the charge carrier is on the order of magnitude of the lattice spacing [12]. On the other hand, the hopping model assumes that the charge is completely localized on a single molecule and moves between adjacent molecules through thermal activation which is not the case for most of the OSCs as their wavefuction could be delocalized over few molecules [13]. Additionally, the hopping transport theory does not consider the non-local charge-phonon coupling.

To accurately model charge end energy transfer in OSCs, it is necessary to consider the interaction between the motion of atomic nuclei and electronic motion beyond the adiabatic regime. Due to the computational complexity of such simulations, various strategies have been developed. One approach involves quantum mechanical treatment of electron dynamics while reducing the dimensionality by either considering a fixed nuclear frame or incorporating only a few nuclear modes. Another approach retains full dimensionality but divides the system into quantum mechanical and classical degrees of freedom. This latter approach, known as Non-adiabatic Mixed Quantum-Classical (NA-MQC) dynamics. These approaches include trajectory surface hopping (TSH), mean-field Ehrenfest (MFE), mixed quantum-classical Liouville equation (QCLE), the mapping approach. Broadly speaking, NA-MQC methods propagate the nuclei or slow particles using classical trajectories [12, 14, 15]. In recent years, on-the-fly NA-MQC dynamics has pushed the boundaries of excited-state computational chemistry, becoming a crucial tool for investigating practical problems in various fields.

Data-driven approaches, such as machine learning (ML) methods, have emerged as valuable tools for predicting charge and exciton transfer properties. In particular, neural network (NN) models have been successfully employed to forecast charge transfer couplings in both organic and metal-organic systems [16–18]. Neural networks have also demonstrated their efficacy in predicting excitation energies in biological systems [19]. Additionally, ML-driven excited-state molecular dynamics have been extensively explored, focusing on small organic molecules [18, 19]. By training ML models on small yet representative datasets, which include relevant electronic parameters obtained from quantum chemistry calculations, it becomes possible to utilize computationally efficient ML models to drive transfer simulations. This offers

a significant advantage over costly on-the-fly quantum chemical calculations, which struggle to handle the computational demands associated with large system sizes and lengthy trajectories needed for accurate prediction of the observable.

In this research we tried to investigate some of the computational challenges of OSCs in terms of charge and energy transfer by employing computational efficient method to model these complex problems. We focused on the propagation of charge and exciton in OSCs using non-adiabatic molecular dynamic simulation methods and the charge phonon interactions that can affect the charge mobility in these material. In addition, we benefit from machine learning technique such as artificial neural networks to accelerate the computation time of the simulations.

2. Theoretical Background

2.1. Electronic Structure Theory

Electronic structure theory in computational chemistry is a powerful framework that enables us to understand and predict the behavior of molecules and materials at the fundamental level of their electronic properties. It forms the foundation for investigating chemical reactions, designing new compounds, and exploring the properties of materials, all without the need for costly and time-consuming experiments. By employing the principles of quantum mechanics and computational methods, electronic structure theory provides a deep insight into the distribution and behavior of electrons within a system.

At its core, electronic structure theory aims to solve the Schrödinger equation, which describes the quantum mechanical behavior of electrons in a given molecular system. However, due to the complexity of this equation, direct analytical solutions are typically not feasible except for the simplest systems. Instead, computational methods are employed to approximate and solve the equation numerically, enabling the investigation of increasingly complex molecular systems.

The starting point of electronic structure theory is the concept of the wave function, which provides a mathematical description of the electronic state of a system. The wave function incorporates information about positions and energies of the electrons, and its square magnitude gives the probability density of finding an electron at a specific location within the system. However, due to the high dimensionality of the electronic wave function, an exact solution for large systems remains elusive.

To address this challenge, various approximation methods have been developed. One commonly used approach is the Hartree-Fock method, which assumes that each electron moves independently within an average field generated by all other electrons. This simplification reduces the problem to

a set of coupled one-electron equations, known as the self-consistent field equations, which can be solved iteratively to obtain an approximate solution for the electronic structure.

Another widely employed approach is density functional theory (DFT), which focuses on the electron density rather than the wave function. DFT relates the energy of a system to its electron density, using the Hohenberg-Kohn theorems, and provides a computationally efficient framework for studying larger systems. Due to the exchange-correlation functional involved in the DFT calculations, this method gives a better description of electron correlation interactions than the HF theory.

Beyond these methods, there exist more advanced techniques such as post-Hartree-Fock methods (e.g., configuration interaction and coupled cluster methods) and more sophisticated variants of DFT (e.g., hybrid functionals and time-dependent DFT). These methods aim to improve accuracy by including higher-order electron correlation effects or by treating time-dependent phenomena.

2.1.1. Schrödinger Equation

The time evolution of a quantum state $|\Psi\rangle$ is represented by the time-dependent Schrödinger equation (TDSE),

$$i\hbar\partial_t|\Psi\rangle = \hat{H}|\Psi\rangle, \tag{2.1}$$

where $|\Psi\rangle$ depends on both electronic and nuclear coordinates. The $\hat{H}$ is the Hamiltonian operator which is a description of the energy of the system. However, the exact solution of the equation 2.1 is limited to the simplest case of a hydrogen-like atom, and accurate numerical solutions for larger systems are difficult to obtain.

2.1.2. Hamiltonian

The fundamental object at the heart of quantum chemistry and condensed-matter physics is the molecular Hamiltonian that describes the total energy

of the system. The Hamiltonian operator for a molecular system consisting of n electrons and k nuclei can be expressed as

$$\hat{H} = \hat{K}_N + \hat{K}_e + \hat{V}_{NN} + \hat{V}_{Ne} + \hat{V}_{ee}. \tag{2.2}$$

The first two terms represent the kinetic energy of the electrons, and nuclei, respectively, while the latter three terms describe the nuclear-nuclear, electron-nuclear, and electron-electron interactions. Each term can be described as follows

$$\begin{aligned}
\hat{K}_N &= -\sum_{j=1}^{k} \frac{1}{2M_j} \nabla^2_{R_j}, \\
\hat{K}_e &= -\frac{1}{2} \sum_{i=1}^{n} \nabla^2_{r_i}, \\
\hat{V}_{NN} &= \sum_{j<j'} \frac{Z_j Z_{j'}}{|R_j - R_{j'}|}, \\
\hat{V}_{Ne} &= \sum_{i,j} \frac{-Z_j}{|r_i - R_j|}, \\
\hat{V}_{ee} &= \sum_{i<i'} \frac{1}{|r_i - r_{i'}|},
\end{aligned} \tag{2.3}$$

where r_i and R_j denote the position of the ith electron and position of the jth nucleus respectively. Z_j is the atomic number of the nucleus, and e is the electronic charge. All the contributions are in atomic units.

Therefore, the total Hamiltonian can be separated into nuclear and electronic components, given by:

$$\hat{H} = \hat{K}_N + \hat{H}_{el}, \tag{2.4}$$

where $\hat{H}_{el}$ is the electronic Hamiltonian, defined as:

$$\hat{H}_{el} = \hat{K}_e + \hat{V}_{ee} + \hat{V}_{Ne} + \hat{V}_{NN}. \tag{2.5}$$

$\hat{H}_{el}$ describes an electron cloud in an external electrostatic potential created by nuclei at fixed positions. The eigenvalue spectrum of $\hat{H}_{el}$ then yields the electronic energy levels E_i, $i = 0, 1, 2, \ldots$ with the electronic states $|\psi_i\rangle$.

$$\hat{H}_{el}|\psi_i\rangle = E_i|\psi_i\rangle, \tag{2.6}$$

This eigenvalue problem is the time-independent electronic Schrödinger equation. The E_i which is a function of nuclear coordinates $E_i(R_1, R_2, \ldots)$ are called potential energy surfaces, as they act as an effective potential for the nuclei.

2.1.3. Born-Oppenheimer Approximation

The Born-Oppenheimer approximation is a fundamental concept in molecular physics and chemistry. It is a method of approximating the total electronic wavefunction of a system by separating the nuclear and electronic motion.

The basic idea behind the Born-Oppenheimer approximation is that the nuclei in a molecule are much heavier than the electrons, and therefore move much slower. This allows us to only consider the evolution of the electronic degrees of freedom in an electrostatic potential field caused by the nuclei at fixed positions. In this way, we can write the total wavefunction of the molecule as a product of electronic and nuclear wavefunctions:

$$\Psi(R, r) = \chi(R)\phi(r) \tag{2.7}$$

Here, R represents the nuclear coordinates and r represents the electronic coordinates. $\chi(R)$ is the nuclear wavefunction, which depends only on the nuclear coordinates, and $\phi(r)$ is the electronic wavefunction, which depends only on the electronic coordinates.

The Born-Oppenheimer approximation allows us to treat the electronic and nuclear motions separately. By solving the electronic Schrödinger equation for a fixed set of nuclear coordinates, we can determine the electronic wavefunction $\phi(r)$. Then, by substituting this electronic wavefunction into the

Schrödinger equation for the nuclear motion, we can determine the nuclear wavefunction $\chi(R)$.

The validity of the Born-Oppenheimer approximation depends on the relative masses of the nuclei and electrons, and the strength of their interactions. In many cases, the approximation works well and provides a good starting point for more sophisticated calculations.

2.1.4. Density Functional Theory

Density Functional Theory (DFT) is a widely used computational method in condensed matter physics, materials science, and chemistry. It is based on the idea that the ground-state properties of a system can be determined by the electron density rather than the wavefunction. The electron density can be calculated using the Kohn-Sham equations, which are derived from the Hohenberg-Kohn theorem and the Kohn-Sham variational principle.

Hohenberg-Kohn Theorem

The first Hohenberg-Kohn theorem states that the ground state electron density uniquely determines the external potential in a quantum mechanical system, and therefore the total energy of the system. This means that the electronic structure of a molecule or material can be described by its electron density alone, rather than by the full wave function of all the electrons in the system, which makes calculations much simpler and more efficient.

The second Hohenberg-Kohn theorem says that the minimum energy is achieved for the true ground state density and all other densities yield higher energies.

Kohn-Sham Equations

The Kohn-Sham equations are based on the idea of separating the many-body problem of the interacting electrons in a system into a set of non-interacting electron problems. The basic idea is to introduce a set of auxiliary non-interacting electrons, called the Kohn-Sham orbitals, which have the same

electron density as the real interacting electrons in the system. The Kohn-Sham orbitals are determined by solving a set of self-consistent equations, known as the Kohn-Sham equations. The Kohn-Sham equations are given by

$$\hat{H}_{KS}\psi_i(\mathbf{r}) = \epsilon_i\psi_i(\mathbf{r}), \tag{2.8}$$

where $\hat{H}_{KS}$ is the Kohn-Sham Hamiltonian, $\psi_i(\mathbf{r})$ is the i-th Kohn-Sham orbital, and ϵ_i is the corresponding Kohn-Sham energy.

The Kohn-Sham Hamiltonian is defined as

$$\hat{H}_{KS} = -\frac{\hbar^2}{2m}\nabla^2 + V\mathrm{eff}(\mathbf{r}), \tag{2.9}$$

where m is the electron mass and $V_{\mathrm{eff}}(\mathbf{r})$ is the effective potential. The effective potential includes the external potential, the Hartree potential from the electron-electron interactions, and the exchange-correlation potential from the exchange and correlation effects.

The electron density is calculated from the Kohn-Sham orbitals as

$$\rho(\mathbf{r}) = \sum_{i}^{occ} |\psi_i(\mathbf{r})|^2, \tag{2.10}$$

where the sum runs over all occupied orbitals.

The Hartree potential is given by

$$V_H(\mathbf{r}) = \int \frac{\rho(\mathbf{r}')}{|\mathbf{r} - \mathbf{r}'|} d\mathbf{r}', \tag{2.11}$$

where $\rho(\mathbf{r}')$ is the electron density at position $\mathbf{r}'$.

The exchange-correlation potential is approximated using a density functional

$$V_{\mathrm{xc}}(\mathbf{r}) = \frac{\delta E_{\mathrm{xc}}[\rho]}{\delta\rho(\mathbf{r})}, \tag{2.12}$$

where $E_{\text{xc}}[\rho]$ is the exchange-correlation energy functional.

The Kohn-Sham equations are solved iteratively until self-consistency is achieved.

Exchange-Correlation Functionals

The exchange-correlation functionals are the most important input for DFT calculations. They approximate the exchange-correlation energy, which is an exact but unknown functional of the electron density.

The local density approximation (LDA) is the simplest exchange-correlation functional, which approximates the exchange-correlation energy as a function of the local electron density at each point in space. The generalized gradient approximation (GGA) includes the gradient of the electron density in addition to the local density. Other more advanced functionals, such as hybrid functionals and meta-GGAs, include additional terms that go beyond the GGA.

2.1.5. Density Functional Tight Binding Method

The Density Functional Tight Binding (DFTB) method is a semi-empirical approach to electronic structure calculations that combines elements of density functional theory (DFT) and tight binding theory [20, 21].

In the DFTB method, the electron density is approximated as a linear combination of atomic orbitals. The coefficients of these atomic orbitals are determined by minimizing the total energy of the system, subject to the constraint that the electron density is equal to the true density. This is achieved by using a density functional that approximates the exchange-correlation energy.

The total energy of the system is given by

$$E_{tot} = E_{el} + E_{nn} + E_{xc}, \tag{2.13}$$

where E_{el} is the electronic energy, E_{nn} is the nuclear-nuclear repulsion energy, and E_{xc} is the exchange-correlation energy.

The electronic energy is given by

$$E_{el} = \sum_{i}^{occ} \sum_{j}^{all} H_{ij}^{DFTB} \rho_{ji} - \frac{1}{2} \sum_{i}^{occ} \sum_{j}^{all} S_{ij}^{DFTB} J_{ij}^{DFTB} \rho_{ji}, \tag{2.14}$$

where H_{ij}^{DFTB} and S_{ij}^{DFTB} are the Hamiltonian and overlap matrix elements, respectively, and ρ_{ji} is the electron density matrix element. The sum over i runs over the occupied orbitals, while the sum over j runs over all orbitals.

The exchange-correlation energy is given by

$$E_{xc} = \int d^3 r \rho(\mathbf{r}) \epsilon_{xc}[\rho(\mathbf{r})], \tag{2.15}$$

where $\rho(\mathbf{r})$ is the electron density and ϵ_{xc} is the exchange-correlation functional.

The DFTB method uses a minimal basis set of atomic orbitals, typically consisting of s and p orbitals. The Hamiltonian and overlap matrix elements are calculated using the Slater-Koster parameters, which describe the overlap and hopping integrals between neighboring atomic orbitals. The Coulomb interaction between electrons is approximated using a truncated multipole expansion.

The accuracy of the DFTB method depends on the choice of parameters used to describe the atomic orbitals and the multipole expansion, which are typically fitted to experimental or high-level theoretical data. Despite its simplified approach, the DFTB method has been shown to provide accurate results for a wide range of systems, including molecular and condensed matter systems.

Self-Consistent Charge SCC-DFTB

The Self-Consistent Charge (SCC) Density Functional Tight Binding (DFTB) method is an extension of the standard DFTB method that includes a self-consistent treatment of the charge density. In the SCC-DFTB method, the electronic density is updated iteratively until self-consistency is achieved [20].

The electron density is still approximated as a linear combination of atomic orbitals, but the coefficients of these atomic orbitals are now determined by minimizing the total energy of the system subject to the constraint that the electron density is self-consistent. The SCC-DFTB method uses a density functional that approximates the exchange-correlation energy and also includes a term that enforces self-consistency.

The total energy of the system is given by

$$E_{tot} = E_{el} + E_{nn} + E_{xc} + E_{sc}, \tag{2.16}$$

where E_{sc} is the self-consistency energy and the rest are the same as non self-consistence DFTB.

The self-consistency energy in the SCC-DFTB method is given by

$$E_{sc} = \frac{1}{2} \int d^3r \int d^3r' \frac{\rho(\mathbf{r})\rho(\mathbf{r}')}{|\mathbf{r} - \mathbf{r}'|}, \tag{2.17}$$

where $\rho(\mathbf{r})$ is the electron density.

Long-Range Corrected Time-Dependent DFTB

DFTB can be formulated as a time-dependent theory, which enables the calculation of non-adiabatic dynamics of molecular excitations with significantly lower computational costs compared to time-dependent variants of DFT. However, the local exchange-correlation (XC) functionals (GGA) used in DFTB do not provide accurate results for large systems and excited states. To address this issue, Niehaus and Della Sala developed a long-range corrected version of the DFTB formalism, which was later combined with the TD-DFTB formalism by Kranz et al. [22] This combined method, known as LC-TD-DFTB, has been demonstrated to perform well in describing photochemical properties in organo-chemical and bio-chemical systems [23–25].

2.2. Molecular Dynamics Simulation

Molecular dynamics (MD) simulation is a powerful computational method that is used to study the motion and behavior of molecules. It is based on the laws of classical mechanics and uses numerical algorithms to integrate the equations of motion for a collection of atoms or molecules. MD simulations have become an essential tool in the study of materials science, chemistry, and biochemistry, providing insight into the structure and function of complex systems that cannot be observed experimentally.

MD simulation consists of solving the classical equations of motion for a collection of atoms or molecules, typically using Newton's second law

$$m_i \frac{d^2 \mathbf{r}_i}{dt^2} = \mathbf{F}_i, \tag{2.18}$$

where m_i is the mass of atom i, $\mathbf{r}_i$ is its position, and $\mathbf{F}_i$ is the net force acting on it. The force acting on the atoms is typically calculated using an inter-atomic potential, which describes the interactions between atoms in the system. The potential can be divided into bonded and non-bonded contributions as

$$U_{total} = U_{bonded} + U_{non-bonded}, \tag{2.19}$$

where U_{bonded} includes the energy associated with bonded interactions, such as covalent bonds, and $U_{non-bonded}$ includes the energy associated with non-bonded interactions, such as van der Waals forces and electrostatic interactions.

2.2.1. Integration Algorithms

To solve the equations of motion, numerical integration algorithms are used to propagate the positions and velocities of the atoms in time. The most commonly used algorithm is the Verlet algorithm, which approximates the equations of motion by updating particle positions and velocities in discrete time steps.

$$\text{Compute force at time } t: \quad \mathbf{F}(t)$$

$$\text{Update position:} \quad \mathbf{r}(t+\Delta t) = 2\mathbf{r}(t) - \mathbf{r}(t-\Delta t) + \left(\frac{\mathbf{F}(t)}{m}\right)\Delta t^2$$

$$\text{Compute force at time } t+\Delta t: \quad \mathbf{F}(t+\Delta t)$$

$$\text{Update velocity:} \quad \mathbf{v}(t+\Delta t) = \frac{\mathbf{r}(t+\Delta t) - \mathbf{r}(t-\Delta t)}{2\Delta t}$$

Repeat the integration loop for the desired number of time steps or until the simulation reaches the desired time.

Other integration algorithms, such as the leapfrog algorithm and the velocity-Verlet algorithm, are also commonly used.

2.2.2. Thermostats and Barostats

MD simulations are typically carried out in the canonical ensemble (NVT) or the isothermal-isobaric ensemble (NPT), where the number of atoms or molecules, volume, and temperature are constant for the former, and the number of atoms or molecules, pressure, and temperature are constant for the latter. To maintain the desired ensemble, thermostats and barostats are used to control the temperature and pressure of the system.

The most commonly used thermostat is the Nose-Hoover thermostat, which adds an additional term to the equations of motion that couples the velocities of the atoms to a heat bath as

$$m_i \frac{d^2\mathbf{r}i}{dt^2} = \mathbf{F}_i - \zeta m_i \mathbf{v}_i, \tag{2.20}$$

where ζ is a friction coefficient that controls the coupling strength. The Nose-Hoover thermostat can be extended to the NPT ensemble by adding a barostat that controls the pressure of the system.

2.2.3. Periodic Boundary Conditions

MD simulations are typically carried out under periodic boundary conditions, where the simulation box is replicated in all directions, creating an infinite lattice of molecules. Periodic boundary conditions allow the simulation of bulk systems and also eliminate surface effects that can arise from finite systems.

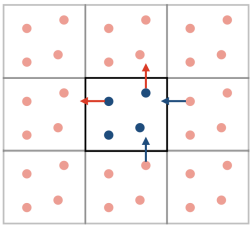

Figure 2.1.: Periodic boundary conditions (PBC) in 2D: The central box is replicated in all directions. As soon as a particle cross the PBC in any direction, its replica would replace it.

2.2.4. Force Fields

In MD simulations, force fields are mathematical models used to describe the inter-atomic interactions within a molecular system. They provide an approximation of the potential energy of the system as a function of the atomic positions. Force fields are essential for simulating the dynamics of molecules and materials, enabling the investigation of their structural, thermodynamic, and kinetic properties.

A typical force field consists of two main components: a bonded potential energy function and a non-bonded potential energy function.

Bonded Potential Energy Function

The bonded potential energy function describes the interactions between atoms connected by chemical bonds in a molecule. It includes terms for bonds, angles, and dihedral angles. The most common functional forms are harmonic potentials for bonds and angles, and periodic potentials for dihedral angles.

The potential energy function for bonds can be represented as

$$E_{\text{bond}} = \sum_{\text{bonds}} K_r (r - r_0)^2, \tag{2.21}$$

where K_r is the bond force constant and r_0 is the equilibrium bond length.

The potential energy function for angles can be represented as

$$E_{\text{angle}} = \sum_{\text{angles}} K_\theta (\theta - \theta_0)^2, \tag{2.22}$$

where K_θ is the angle force constant and θ_0 is the equilibrium bond angle.

The potential energy function for dihedral angles can be represented as

$$E_{\text{dihedral}} = \sum_{\text{dihedrals}} V_n (1 + \cos(n\phi - \gamma)), \tag{2.23}$$

where V_n is the amplitude, n is the periodicity, ϕ is the dihedral angle, and γ is the phase shift.

Non-bonded Potential Energy Function

The non-bonded potential energy function describes the interactions between atoms that are not directly bonded. It consists of two components: the van der Waals potential and the electrostatic potential.

The van der Waals potential energy function can be represented as

$$E_{\text{vdW}} = \sum_{\text{pairs}} \left(4\epsilon \left(\left(\frac{\sigma}{r} \right)^{12} - \left(\frac{\sigma}{r} \right)^{6} \right) \right), \tag{2.24}$$

where ϵ is the depth of the potential well and σ is the distance where the potential is zero, and r is the distance between atom pairs.

The electrostatic potential energy function can be represented as

$$E_{\text{elec}} = \sum_{\text{pairs}} \left(\frac{1}{4\pi\epsilon_0} \frac{q_i q_j}{r} \right), \tag{2.25}$$

where q_i and q_j are the charges of atom pairs, ϵ_0 is the vacuum permittivity, and r is the distance between atom pairs.

Combining Bonded and Non-bonded Potentials

The total potential energy of the system is given by the sum of the bonded and non-bonded potential energy functions as

$$E_{\text{total}} = E_{\text{bond}} + E_{\text{angle}} + E_{\text{dihedral}} + E_{\text{vdW}} + E_{\text{elec}}. \tag{2.26}$$

The force acting on each atom can be calculated by taking the negative gradient of the potential energy with respect to the atom's position as

$$\mathbf{F} = -\nabla E_{\text{total}}. \tag{2.27}$$

There are different types of force fields commonly used in Molecular Dynamics (MD) simulations. Empirical force fields are the most widely used force fields in MD simulations. They are derived from experimental data and/or quantum mechanical calculations. Popular empirical force fields include CHARMM which is widely used for biomolecular simulations and has parameters for proteins, nucleic acids, lipids, and carbohydrates. Moreover, AMBER [26] and OPLS [27] force fields from this type are extensively used for biomolecular, Liquids, and organic molecules. Another type of force fields are called polarizable force fields which take into account the polarization effects of atoms and molecules. These force fields include parameters that allow the partial charges of the atoms to vary in response to their local environment.

2.3. Quantum Mechanics/Molecular Mechanics (QM/MM)

In QMMM simulations, the system is divided into two parts: the quantum mechanical region (QM), which represents the active region of interest and is treated using quantum mechanics, and the molecular mechanical (MM) region, which represents the surrounding environment and is treated using classical mechanics.

In our QM/MM approach where the propagation of the charge and exciton in OSCs are considered, we take it a step further by simplifying the depiction of the charge carrier, focusing only on a few frontier orbitals surrounding the Fermi level, such as the highest occupied molecular orbitals (HOMOs) in hole transfer, and the lowest unoccupied molecular orbitals (LUMOs) in electron transfer. The wave function $|\Psi\langle$ that characterizes the state of the charge carrier is then expressed as a linear combination of frontier orbitals. Therefore, our approach goes beyond the standard QM/MM separation, freezing not only spatially, but also energetically isolated states from the orbitals that are critical for charge transport. Furthermore, the energy of the quantum mechanical (QM) region that does not possess any additional charge is estimated using molecular mechanics (MM) and incorporated into the overall MM energy [15]. This results in the total energy value for the hole as the charge carrier as

$$E^{+} \equiv E_{MM}^{tot} - \langle\Psi|H[\rho_0]|\Psi\rangle + \Delta E_{QM/MM}, \tag{2.28}$$

Here, the symbol $\Psi\rangle$ represents the wave function of the hole, $H[\rho_0]$ denotes the Kohn-Sham Hamiltonian of the uncharged system, and $\Delta E_{QM/MM}$ refers to the interaction energy between the QM and MM subsystems.

2.3.1. Fragment Orbital Approximation

In comparison to inorganic semiconductors, which are covalently bound, organic semiconductors have interactions that are driven by noncovalent forces. As a result, the electronic structure of the QM zone can be simplified conceptually using a coarse-grained Hamiltonian [28].

The wave function of the hole in OSCs can be represented as a linear combination of molecular orbitals $|\Phi_m\rangle$ from fragment molecules A, which have been orthogonalized.

$$\Psi = \sum_{A} \sum_{m \in A} c_m |\Phi_m\rangle \tag{2.29}$$

Φ_m in equation 2.29 represents the molecular orbitals of the individual fragments. Therefore, the total energy of a system in fragment orbital basis with a hole as the charge carrier is obtained by inserting the equation 2.29 into equation 2.28:

$$\begin{aligned} E^{+} &= E^{0} + \sum_{A,B} \sum_{m \in A} \sum_{n \in B} c_m^{*} c_n H_{mn}^{0} + \Delta E_{QM/MM} \\ H_{mn}^{0} &= \langle \Phi_m | H[\rho_0] | \Phi_n \rangle \\ \Delta E_{QM/MM} &= \sum_{k} \sum_{m \in A} |c_m^2| \sum_{k} \sum_{a \in A} \frac{\Delta q_a^m q_k^0}{|R_a - R_k|} \end{aligned} \tag{2.30}$$

E_0 in the above equation is the energy of the neutral system and H_{mn}^0 is fragment orbital (FO) Hamiltonian. The $\Delta E_{QM/MM}$, is the QM/MM interaction, where q_k^0 is the partial charge on atom k of the neutral environment, and Δq_a^m is the change of the Mulliken charge on atom a due to a hole located at orbital m

2.4. Non-adiabatic Molecular Dynamics

Born-Oppenheimer approximation (BOA) is generally applicable for the systems in their electronic ground state, but it fails when the electronic states are strongly coupled. Many processes such as charge and exciton transfer which is the topic of this research involve several strongly coupled PESs [29].

Non-adiabatic molecular dynamics (NAMD), is a computational method that allows for the simulation of the dynamics of molecules in the presence of non-adiabatic effects. In these methods, the electronic structure is described by the time-dependent Schrödinger equation, which is coupled to the classical

equations of motion for the nuclei. The coupling between the electronic and nuclear degrees of freedom is represented by the non-adiabatic coupling matrix elements (NACEs), which quantify the strength of the interaction between electronic states.

NAMD simulations require significantly more computational resources than adiabatic MD simulations, due to the inclusion of the electronic degrees of freedom. However, there are efficient methods for this aim that we have used in this research.

Ehrenfest Mean Field

In the Ehrenfest mean field (EMF) approach the evolution of the classical nuclear degrees of freedom is governed by the gradient of the expectation value of the systems total energy.

Applying equation 2.29 into TDSE we obtain:

$$\dot{c}_m = -i \sum_n H_{mn} c_n - \sum_n c_n \langle \Phi_m | \dot{\Phi}_n \rangle. \tag{2.31}$$

Which describes the propagation equation for the expansion coefficients. In equation 2.31, where H_{mn} are the Hamiltonian matrix elements including the QM/MM interactions. The last term indicated the non-adiabatic coupling between molecular orbitals m and n, which is negligibly small for molecules far apart because of the exponential decay of the molecular orbital. Therefore, the dynamics of the nuclei becomes:

$$m_k \ddot{R}_i = -\frac{\partial E^0}{\partial R_i} + \sum_{mn} c_m^* c_n \frac{\partial H^0_{mn}}{\partial R_i} - \frac{\partial \Delta E_{QM/MM}}{\partial R_i} \tag{2.32}$$

Where, i represents the x, y, and, z coordinates of the atom k. In fact, the equation 2.32 indicates that the classical degrees of freedom move on a single averaged potential energy surface (PES).

Trajectory Surface Hopping

Trajectory surface hopping (TSH) is a fascinating approach to study non-adiabatic physical phenomena such as the charge and exciton transfer in organic semiconductors as it is shown that the standard models (band theory and Markus theory) do not provide proper result for this class of material because of the nature of their intermolecular interactions. TSH has been reviewed by several researchers [30]. Here we summarize the outlines of the theory.

In the TSH theory the wavefunction is expressed as the linear combination of the adiabatic states:

$$\Psi(t) = \sum_i C_i^{ad}(t)|\psi_i(R(t))\rangle \tag{2.33}$$

By plugging this wavefunction into the TDSE, we obtain the time evolution of the wavefunction from the expansion coefficient

$$i\hbar\dot{C}_i^{ad}(t) = \sum_j C_i^{ad}(t)(H_{ij}^{ad} - i\hbar d_{ij}^{ad}) \tag{2.34}$$

Where the H_{ii}^{ad} is the potential energy, corresponding to the adiabatic state i. Adiabatic Hamiltonian can be obtained from a unitary transformation as bellow:

$$\mathbf{H^{ad}} = \mathbf{U}\mathbf{H^0}\mathbf{U}^\dagger \tag{2.35}$$

d_{ij}^{ad} are the adiabatic coupling elements NACEs which are derived using the chain rule.

$$d_{ij}^{ad} = \langle\psi_i|\frac{d\psi_j}{dt}\rangle = \dot{\mathbf{R}}\mathbf{d}_{ij}^{ad} \tag{2.36}$$

The bold $\mathbf{d}_{ij}^{ad}$ in the equation 2.36, denotes the non-adiabatic coupling vector (NACVs) which is given as [30]:

$$\mathbf{d}_{ij}^{ad} \approx \frac{[\mathbf{U}^{\dagger}\nabla\mathbf{H}^{0}\mathbf{U}]}{H_i^{ad} - H_j^{ad}} \tag{2.37}$$

Then classical trajectories evolve on a single adiabatic energy surface based on Newton second law

$$m_I\ddot{\mathbf{R}}_I = -\nabla_I E_i \tag{2.38}$$

Where m_I and $\mathbf{R}_I$ are mass and position of the atom I respectively.

The hopping from state i to state j is determined by the comparison of the transition probabilities $P_{i\to j}$ In the fewest switches surface hopping (FSSH) algorithm, the main objective is to reduce the number of surface hops while maintaining internal consistency. This is achieved by allowing a transition between potential energy surfaces only when the currently occupied state shows a decrease in population [12]. The probability of hopping from the state i to state j is determined as follows:

$$P_{i\to j} = max\left\{0,\ 2d_{ij}\frac{Re(C_j^{ad^*}C_i^{ad})}{|C_i^{ad}|^2}\Delta t\right\} \tag{2.39}$$

Hopping event from the state i to state k occurs if:

$$\sum_{j=1}^{k-1} P_{i\to j} < \zeta \leq \sum_{j=1}^{k} P_{i\to j} \tag{2.40}$$

Where ζ is a pseudorandom number in $[0, 1]$.

In order to maintain the conservation of total energy for each trajectory, adjustments to the nuclear momenta are required when a hop occurs. Typically, this is accomplished by rescaling the nuclear velocities to counterbalance the change in potential energy (PE). While it is possible to evenly distribute this effect across all velocity components, better results are obtained when the velocities are rescaled in alignment with the non-adiabatic coupling vectors [31]. However, if the momentum adjustment proves insufficient to compensate for the PE change (known as an "energy-forbidden" or "frustrated" hop),

the trajectory will persist in the original electronic state j, and the momenta along the non-adiabatic coupling vectors will be reversed.

Instead of relying on non-adiabatic coupling vectors (NCVs), an alternative method involves adjusting the hopping probability by applying the Boltzmann factor, while keeping the velocities unchanged. This Boltzmann-corrected FSSH method offers the advantage of avoiding the computational complexity associated with NCVs, while still producing superior results compared to isotropic re-scaling [14, 32].

After a hop occurs, the fragments occupied by the charge carrier need to respond to the changed electronic state by relaxing their geometry, resulting in a decrease in their site energies. This can be achieved in two ways: either by artificially lowering the site energy by a predetermined value for the reorganization energy, or by incorporating the forces stemming from the charged state. It's important to note that this approach differs from other non-adiabatic dynamics methods, as it does not rely on adiabatic forces.

2.5. Charge and Exciton Transfer

2.5.1. Charge Transfer Regimes

Hopping Regime and Marcus Theory

The hopping transport model is a common approach for modeling charge transport in organic semiconductors. This model assumes that the charge carrier is localized on a site within the material and moves from one site to another through a series of discrete jumps. The degree of localization varies depending on the nature of the molecules, which can range from a single molecular unit to a collection of molecules. There are few distinct mechanisms that can induce localization in these systems. One mechanism is small polaron theory, which assume that the charge carrier interacts with its medium and induces a local nuclear distortion of the molecular site and its environment. These phenomena can stabilize the charge and form a quasi-particle known as a small polaron. Alternatively, localization could be induced by thermal fluctuations of the coupling between sites, referred to as non-local electron-phonon coupling [33, 34].

In general, models based on hopping describe the transfer of electric charge through the movement of discrete charge carriers that jump between specific sites. These jumps occur according to charge transfer rates k_{ET} that are specific to each site and direction, and are influenced by the relative geometry of the initial and final orbitals.

Marcus' theory provides a way to describe the rate at which electrons move between different molecules in an organic semiconductor. The theory describes the electron transfer rate as a function of the energy difference between the donor and acceptor molecules, as well as the reorganization energy of the system. The reorganization energy describes the amount of energy required to reconfigure the system during the electron transfer process.

In Marcus theory, the rate of electron transfer between two molecules is described by the following equation:

$$k_{ET} = \frac{2\pi}{\hbar}|V_{DA}|^2 \frac{1}{\sqrt{4\pi\lambda k_B T}} e^{-\frac{\Delta G^\circ + \lambda}{4\lambda k_B T}} \tag{2.41}$$

Where k_{ET} is the electron transfer rate, $\hbar$ is the reduced Planck constant, $|V_{DA}|$ is the electronic coupling between the donor and acceptor molecules, λ is the reorganization energy of the system, k_B is the Boltzmann constant, T is the temperature, and ΔG° is the free energy change associated with the electron transfer reaction under standard conditions [35, 36].

One key parameter in our charge transfer calculation algorithm is the electronic coupling. In this work, the calculation of electronic couplings was performed using the semi-empirical Tight-Binding Density Functional theory (DFTB) [20]. Compared to standard GGA-DFT methods with medium-sized basis sets, this method is roughly 2-3 orders of magnitude faster. As a result, even molecules containing 92-100 atoms can be calculated in a reasonable amount of time which enables the computation of extensive scans for big systems and the sampling of conformational space.

The calculation of charge transfer couplings involves the separation of the complex into individual molecular fragments. For each fragment, the molecular orbitals φ_m^i are expressed as the linear combination of the atomic orbital basis χ_μ with expansion coefficients c_μ^{im}.

$$\varphi_m^i = \Sigma_\mu c_\mu^{im} \chi_\mu \tag{2.42}$$

Usually, it is sufficient to consider only one orbital (either the HOMO for hole transfer or the LUMO for electron transfer) per fragment. However, in special cases, additional orbitals (such as HOMO-1) can also be taken into account, particularly if the energy difference between the orbitals is small. The Hamiltonian matrix is constructed from the fragment orbital coefficients. For example, for the coupling of the HOMO orbitals, the Hamiltonian is given by

$$H_{mn} = \langle \varphi_m^{HOMO} \mid \hat{H} \mid \varphi_n^{HOMO} \rangle = \Sigma_\mu \Sigma_\nu c_\mu^{HOMO^m} c_\nu^{HOMO^n} \bar{H}_{\mu\nu} \tag{2.43}$$

Where $\bar{H}_{\mu\nu}$ is the Hamiltonian in the atomic-orbital basis. The off-diagonal elements of the Hamiltonian matrix represent the electronic couplings between the individual fragments, while the diagonal elements correspond to the orbital energies. In this work, DFTB+ program was used to calculate the coefficients [21].

The method has been benchmarked against high-level ab initio methods and has been found to reproduce the couplings with high accuracy [37, 38], after an appropriate choice of basis functions and introduction of a scaling parameter, which corrects for the well known DFT deficiencies.

This method has been used to simulate charge carriers in a variety of systems, including organic semiconductors, DNA, and proteins, in close agreement with experimental results [39–44]. Moreover, it has been shown that, employing this method together with trajectory surface hopping approach can be an efficient way to simulate the propagation of charge in the organic semiconductors which results in charge mobility close to experiment measurements [11, 12, 14].

The reorganization energy λ is defined as the sum of the energy required to rearrange the system before the electron transfer and the energy released during the process. It can be calculated as:

$$\lambda = \lambda_{in} + \lambda_{out} \tag{2.44}$$

Where λ_{in} is the internal reorganization energy, which describes the energy required to rearrange the donor and acceptor molecules before the electron transfer, and λ_{out} is the external reorganization energy, which describes the

energy released by the solvent or other external factors during the electron transfer.

Band Regime

In the realm of condensed matter, charge transport is commonly discussed in two opposing regimes: charge hopping and band theory. While hopping assumes that charges are localized on specific sites, band theory proposes that charge carriers are spread out over periodic carrier bands. Band transport has been extensively studied, particularly in the field of inorganic semiconductor research, which has made significant advancements in refining band models over time. Despite some differences in crystal structure, including a mix of covalent and dispersive forces, highly pure organic semiconductors can be studied using these band models. The foundation of band theory lies in Bloch's theorem, which describes the form of an electron orbital in a periodic potential as a combination of plane waves adjusted by a set of periodic functions.

In this theory, the electrons in a solid are treated as waves that are described by their wave vector and energy. The allowed energy levels of these waves form bands, which are separated by gaps of forbidden energies known as band gaps.

In the simplest case, the band theory assumes that the atoms in a solid are arranged in a regular lattice, with each atom contributing one or more valence electrons to a pool of electrons that are shared by all the atoms. These valence electrons form energy bands that are separated by band gaps, with the lowest energy band being called the valence band and the highest energy band being called the conduction band. The electrons in the valence band are bound to the atoms and cannot move freely through the material, while the electrons in the conduction band are free to move and can conduct electricity.

The band gap determines whether a material is a conductor, an insulator, or a semiconductor. Metals have a small or zero band gap, which allows electrons to move freely and makes them good conductors of electricity. Insulators have a large band gap, which prevents electrons from moving freely and makes them poor conductors of electricity. Semiconductors have a small band gap that can be easily modified by doping, allowing them to conduct electricity under certain conditions.

Intermediate Regime

In the study of charge transport in organic solids, there are instances where neither the hopping model nor the band theory model can fully explain the mechanism at play. These cases represent an intermediate regime where the charge carrier is not localized to a specific site nor fully spread out across a carrier band.

When examining the electronic and electron-phonon coupling in these intermediate regimes, we can observe unique behaviors. For example, in some cases, the charge carrier may be localized to a specific region but still have some delocalization, resulting in a partial carrier band. Alternatively, the charge carrier may be spread out over a broad region but still have some localization, leading to a partially hopping-like mechanism.

Understanding these intermediate regimes is important in developing a more comprehensive understanding of charge transport in organic solids. As these materials have potential applications in areas such as electronics, photovoltaics, and optoelectronics, a better understanding of their charge transport mechanisms can lead to the development of more efficient and effective devices.

2.5.2. Exciton Transfer

An exciton can be transferred from an excited "donor" molecule to an "acceptor" molecule through a non-radiative process known as energy transfer. This transfer can occur via two mechanisms: Förster (through-space) or Dexter (through-bond) mechanisms. Förster resonant energy transfer (FRET) relies on dipole-dipole electromagnetic interaction and takes place when the emission spectrum of the donor significantly overlaps with the absorption spectrum of the acceptor. FRET efficiency decreases as the distance between the donor and acceptor increases, typically observed within the range of 1-5 nm. Singlet excitons are typically transferred through Förster mechanism.

In contrast, Dexter energy transfer involves the actual exchange of electrons between the donor and acceptor. This mechanism occurs when the donor and acceptor are approximately 1 nm apart, resulting in a significant overlap

of molecular orbitals. The probability of Dexter energy transfer decreases exponentially with increasing distance between the donor and acceptor. Singlet and triplet excitons can both be transferred through this mechanism.

When the binding energy between an electron and a hole in an exciton is surpassed, they can be separated. This separation is particularly efficient at the interface with an electron-accepting material. If the energy level of the acceptor's lowest unoccupied molecular orbital (LUMO) is significantly lower than that of the excited donor molecule, electron transfer from the donor to the acceptor can take place. This process, known as charge transfer, involves a short-range interaction and occurs when there is a significant spatial overlap between the wavefunctions of the donor and acceptor molecules. As a result of electron transfer, the donor becomes positively charged, and the acceptor becomes negatively charged. Hole transfer is also possible when the energy levels of a donor and an acceptor are properly aligned. The physical mechanism underlying hole transfer is the same as that of electron transfer [45].

2.6. Machine Learning

Machine learning (ML) has become a valuable tool for solving problems that lack an exact mathematical formulation or interpretation, while traditional programming has been successful in tackling logic, algebra, geometry, and optimization problems by providing a function to solve them. The primary distinction between traditional programming and ML lies in their inputs and desired outputs. Traditional programming provides an input and program to obtain a result, whereas ML requires the input and desired output and aims to produce a program as output.

ML tasks encompass regression and classification. Regression tasks seek to find a function that maps variables with a direct relationship, aiming to establish patterns between them. On the other hand, classification tasks assign discrete class labels to examples by optimizing a model that maps input vectors to target values representing different classes.

In the field of machine learning, various statistical methods are employed to extract patterns from data. Supervised learning methods are utilized when data exhibits a clear input-target relationship, such as predicting a molecule's

energy based on its geometry or classifying a compound as drug-like or not. Unsupervised learning methods, on the other hand, are employed to uncover structure and patterns in large datasets without a reference for optimal solutions. This type of learning can be employed to analyze molecular dynamics trajectories and extract different intermediate states represented by geometries. Dimensionality reduction, another form of unsupervised learning, extracts relevant features from high-dimensional inputs, making it useful for analyzing molecular dynamics simulations and pre-processing data for other ML models.

Supervised ML models are parametrized functions that map inputs (x) to targets (y), adjusting their parameters (w) using reference data points to accurately replicate the input-target relationship. The complexity of relationships that a model can handle is determined by its function's shape. Linear regression models, for instance, cannot accurately capture nonlinear behavior, while neural networks with millions of parameters can describe highly complex dependencies.

ML models are capable of solving both regression and classification problems. Regression models use one or multiple independent input variables (features) to quantitatively predict the target(s), which can be one or multiple dependent variables. The commonly used approach for regression is fitting a line to a set of measurements using the least-squares method. On the other hand, classification problems arise when the target is not a continuous variable, but rather a discrete property. For example, identifying specific objects within images is a classification problem frequently encountered in the development of autonomous vehicles.

2.6.1. Artificial Neural Networks

Artificial Neural Networks (ANNs) are powerful computational models inspired by the structure and functionality of the human brain. They have gained significant attention and become a fundamental component of machine learning and artificial intelligence. ANNs are designed to process and analyze complex data, learn patterns, and make predictions or decisions based on the acquired knowledge.

The basic building block of an ANN is an artificial neuron, also known as a perceptron. A perceptron takes multiple inputs, applies weights to each

input, sums them up, and passes the result through an activation function to produce an output. This mimics the behavior of a biological neuron, which receives signals from multiple dendrites, processes them in the cell body, and generates an output signal along the axon.

To represent an artificial neuron mathematically, we can use the following formula in LaTeX format:

$$y = f\left(\sum_{i=1}^{n} w_i \cdot x_i + b\right) \tag{2.45}$$

Here, y represents the output of the neuron, $f(\cdot)$ is the activation function, w_i are the weights associated with each input x_i, n is the total number of inputs, and b denotes the bias term. The activation function introduces non-linearity into the neuron's output, allowing it to model complex relationships between inputs and outputs.

By interconnecting multiple neurons, ANNs form intricate networks of layers. The most common architecture is the feedforward neural network, where neurons are organized into layers, and information flows from the input layer through one or more hidden layers to the output layer. Each neuron in a layer receives inputs from the previous layer and produces an output that serves as an input for the next layer.

The weights and biases in an ANN are learned through a process called training. During training, the network is presented with a set of input-output pairs, and the weights are adjusted iteratively to minimize the difference between the predicted outputs and the desired outputs. This optimization process is typically accomplished using a technique called backpropagation, which calculates the gradients of the network's error with respect to the weights and biases.

The power of ANNs lies in their ability to learn complex patterns and generalize from training data to make accurate predictions or classifications on new, unseen data. They have demonstrated remarkable success in various domains, including image and speech recognition, natural language processing, and data analytics.

3. Charge Transfer in Surface-functionalized Metal Organic Frameworks

Reprinted in parts with permission from
R. Haldar, M. Kozlowska, M. Ganschow, S. Ghosh, M. Jakoby, H. Chen, F. Ghalami, W. Xie, S. Heidrich, Y. Tsutsui, J. Freudenberg, S. Seki, I. A. Howard, B. S. Richards, U. H. F. Bunz, M. Elstner, W. Wenzel and C. Wöll
Interplay of structural dynamics and electronic effects in an engineered assembly of pentacene in a metal-organic framework
Chem. Sci., 2021, 12, 4477 DOI: 10.1039/D0SC07073D

3.1. Introduction

The determination of structure-property relationships in organic semiconductors (OSCs), which are promising materials for thin-film organic field-effect transistors [46–48] is often hampered by the lack of structural order. Aggregated OSC materials are very often amorphous or exhibit rather small structural coherence lengths, resulting in high defect densities. Charge carrier mobility, an important figure of merit of organic semiconductors, is not only affected by the electronic coupling between adjacent chromophores [49] but also by the coupling to vibrations within the molecular aggregates [50–52]. These dynamic effects have emerged as a main bottleneck to improve the mobility in stacked organic semiconductors [53]. Nevertheless, information on the interplay of these factors is scarce. In addition, rational optimization is hampered by the fact that the variations of the molecular core, aimed at the reduction of the amplitudes of the most important vibrations, also changes the crystal structure and the other relevant vibrational modes for the semiconducting performance. It would therefore be of interest to investigate

structurally well-defined model systems where planar, aromatic molecules are packed into crystalline arrangements with a high degree of structural control and low defect density. This can offer independent control over the molecular arrangement and reduce the vibrational degrees of freedom of the system [54–57].

An interesting case is that of pentacene (PEN), an OSC with charge carrier mobilities as high as those of amorphous silicon, which features a highly rigid core. Although mobilities of bulk PEN single crystals are fairly large, it has been speculated that these values may be enhanced further when the relative orientations of the aromatic plane are modified. Variation of side-groups and growth conditions yields herringbone or cofacial (brick-wall, slipped or cofacial) stacks of the aromatic cores with variable charge carrier mobilities [58, 59]. Employing the existing methods of PEN film preparation, often polycrystalline films with the coexistence of more than one crystalline phase are obtained [60]. As a result, establishing structure-property correlations is not straightforward. In particular structural defects hamper the determination of intrinsic properties. It has been shown that the charge carrier mobilities in condensed phases of PEN varies by one order of magnitude depending on preparation conditions.

A robust strategy to engineer the packing of OSCs into highly ordered columns with strong electronic coupling between the aromatic cores is metal-organic frameworks (MOFs) based structures [11]. MOFs exhibit a high degree of structural order and modularity [61–63].

It has been demonstrated that in SURMOF structure (Zn-PEN) the PEN units are arranged in a parallel fashion with high crystalline order. As evidenced by a thorough photophysical characterizations and a density functional theory (DFT) analysis, this molecular arrangement yields strong inter-PEN electronic coupling. Interestingly, instead of the expected band-like charge transport, the Zn-PEN SURMOFs exhibited an intrinsic hopping-like photo-generated charge (hole) carrier mobility of -0.03 $cm^2V^{-1}s^{-1}$ at 300 K with an activation energy of -64 meV. In the context of a prevailing theory of charge transport, strong fluctuations of the intermolecular couplings often play a key role and strongly reduce the hypothetical, large mobility predicted for static arrangements. Our theoretical results confirmed that transport mechanism along the 1D PEN stacks is largely governed by dynamic contributions, arising from rotations of the PEN linkers around the 6,13-axis defined by the two

metal-coordinating carboxylate groups. This frustrated rotation causes fluctuations of the inter-PEN electronic coupling and dynamic disorder, resulting in partial hole delocalization and charge transport mechanism at the borderline between the localized hopping and delocalized charge transport. With the insights from the detailed static and dynamic quantum-mechanical investigations, we identified key principles governing the charge carrier properties of such arrayed columns of OSC compounds.

3.2. Methodology

In order to reproduce experimental results, we used the fewest switches surface hopping FSSH algorithm described in 2.4 to propagate the charge carriers through the Zn-PEN and PEN. Since this approach does not impose any constraints on the wavefunction of the charge carriers as in the band-theory and also no further assumption about the transport mechanism, it can describe both, localized and delocalized charge transports, which depends on the molecular structure of the system, and also can reproduce the temperature dependency of the transport to a very good accuracy [64, 65].

In this method the hole wavefunction is expanded in a set of molecular orbitals from the individual molecules, propagating according to the Schrödinger equation, while the nuclei dynamics follows the Newton's classical equations of motion. Classical and quantum approaches are coupled using a quantum mechanics/molecular mechanics (QM/MM) approach [12]. The details of the method could be found in chapter 2.

3.2.1. System Preparation

In order to generate the simulation box for the Zn-PEN, as the first step in our NAMD approach to calculate the hole mobility, a supercell elongated in [001] direction (z-axis) was made using the X-ray measured unit cell of Zn-PEN SurMOF. It has been shown that in the [001] direction 3.1, the closest C-C distance among the PEN linkers can be 0.38 nm, which causes a strong $\pi - \pi$ interaction and consequently a strong electronic coupling [11].

In order to compare the value of the hole mobility in the Zn-PEN [001] direction with its value in the PEN crystal pi-stack direction, we generated a

simulation box of the PEN crystal elongated in x-axis, figure 3.1 b), using the PEN unitcell.

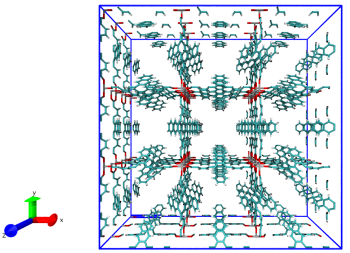

a)

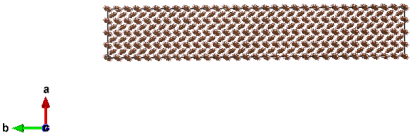

b)

Figure 3.1.: Supercell of a) Zn-PEN and b) PEN

For both systems, the force field parameters were obtained from the general AMBER force field (GAFF) [66, 67] and atomic charges were calculated by restrained electrostatic potential fitting procedure (RESP) [68, 69] with HF/6-31G* [70, 71] level of theory using Gaussian 16 software [72]. After energy minimization the initial structures were equilibrated for 1 ns at 300K in NVT ensemble using Nose-Hoover thermostat [73]. After equilibrating, the simulation were continued for another 0.5 ns and structures were sampled every 10 ps, which required for our trajectory surface hopping and Ehrenfest mean field (EMF) calculation of charge transfer algorithm explained in chapter 2. In order to propagate the hole wavefunctiuon, 30 molecules in z direction of the Zn-PEN crystal and b direction in PEN, where molecules are lined face to face, were chosen to be in the QM-zone. For the case of the Zn-PEN crystal we only considered the PEN linker in the QM-zone and the metal hob is treated classically using force field. The hole wavefunction was initially localized on

the first molecule. We used a time step of 0.100 fs for the propagation of nuclei, the TDSE was integrated numerically with the fourth-order Runge-Kutta algorithm with an integration time step of 0.010 fs.

3.2.2. Mean Squared displacement (MSD) and Hole Mobility

Mean squared displacement (MSD) were calculated from its average value over 600 trajectories, which were simulated for 1 ps each. The diffusion constant of the hole was calculated from the MSD according to the following equation

$$\begin{aligned} D &= \frac{1}{2n} \lim_{t\to\infty} \frac{dMSD(t)}{dt}. \\ MSD(t) &= \frac{1}{N_{traj}} \sum_{l}^{N_{traj}} \sum_{A} (x_A(t)^{(l)} - x_0^{(l)})^2 P_A(t)^{(l)}, \end{aligned} \tag{3.1}$$

where n is the dimensionality which is set to one in our calculations. $x_A(t)^{(l)}$ and $P_A(t)^{(l)}$ are the center of mass of molecule A and the corresponding diabatic population along the trajectory l, respectively. $x_0^{(l)}$ is the center of charge at $t = 0$.

The charge carrier mobility is calculated with the Einstein-Smoluchowski relation

$$\mu = \frac{eD}{K_B T}, \tag{3.2}$$

where K_B is the Boltzmann constant, e is the elementary charge, and T is temperature and D is the diffusion coefficient.

3.3. Results and Discussions

3.3.1. Charge Transfer

Table 3.1 summarizes the calculated charge transfer results of the two investigated systems. The average value of the hole coupling $\langle J \rangle$, is calculated based

on the equation 2.43 using DFTB, for a dimer coordinate sampled during a course of MD simulation every 1 fs, for the 100 ps. The hole reorganization energy is calculated using DFTB, based on the 4-points scheme (chapter 2). As we only considered the PEN part of the Zn-PEN to be involved in the QM-zone of the NAMD calculations, the reorganization energy of the two investigated systems are the same (93 meV). We find a slightly higher average coupling for the PEN coupling in a crystal. The standard deviation of the couplings is of 15 meV for PEN, while it is 27 meV for Zn-PEN table. This indicates, that we would expect a higher mobility in PEN, since the average coupling is higher and the fluctuations are smaller. And indeed, the predicted hole mobility of Zn-PEN is almost 2 times smaller than its value for the PEN crystal, 1.97 $cm^2V^{-1}s^{-1}$vs 4.15 $cm^2V^{-1}s^{-1}$. The latter value is in good agreement with the experimental estimates for PEN of 5 $cm^2V^{-1}s^{-1}$.

	λ	J	J_{std}	μ_{FSSH}	μ_{EMF}	IPR_{FSSH}	C
Zn-PEN	93	30	27	1.97	2.91	2.17	0.55
PEN	93	36	15	4.15	6.79	2.64	0.85

Table 3.1.: Transport parameters of the Zn-PEN and PEN crystal. The value of the hole coupling and the reorganization energy is in [meV] and mobility is represented in $cm^2V^{-1}s^{-1}$

Consistent to this, we found that the inverse participation ratio (IPR), indicating the degree of the charge delocalization in the system, is 2.17. This means that the charge is delocalized over ca. 2 PEN molecules. This is only slightly lower than in the case of the PEN crystal, where IPR equals to 2.64, i.e., in none of the materials we expect a pure hopping mechanism since the charge carrier is slightly delocalized.

3.3.2. Hole Coupling Fluctuations

The lower mobility, therefore, correlates with a lower average coupling and larger fluctuations, which indicate that the reason for the lower conductivity may be attributed to two factors: a larger intermolecular distance and larger structural fluctuations. Molecular fluctuations of PEN, both in Zn-PEN and PEN crystal, are depicted in figure 3.2. It is clearly seen that the fluctuations of the PEN in Zn-PEN are larger, which should impact the intermolecular interactions and overlap between the molecules. Therefore, the calculated

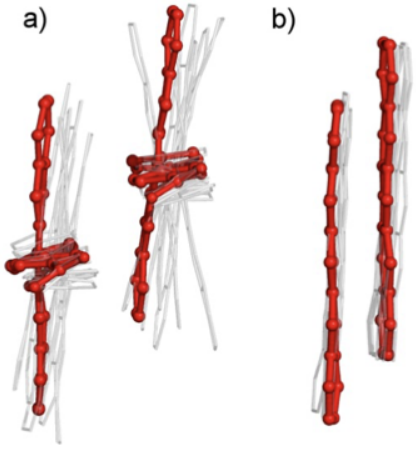

Figure 3.2.: Superposition of the PEN dimers in Zn-PEN (a) and PEN crystal (b) sampled during QM/MM molecular dynamics simulations at 300 K

electronic coupling of the extracted dimer fragments was calculated for the corresponding MD snapshots figure 3.3.

Larger structural fluctuations of the dynamical moves of the PEN linkers in Zn-PEN at 300 K directly impact the electronic coupling, introducing the deviation of 27 meV to the average electronic coupling of 30 meV. It is higher than in the comparison to the average value of coupling (36 meV) and the standard deviation (15 meV) of the PEN crystal. This dependency can be quantitatively analyzed by the coherence parameter.

$$C = \frac{\langle T_{DA} \rangle^2}{\langle T_{DA} \rangle^2 + \langle \delta T_{DA}^2 \rangle}, \tag{3.3}$$

where $\langle \delta T_{DA}^2 \rangle$ is the mean square deviation. Therefore, coherence parameter fails in the range between zero and one, when one means that the effective electronic coupling can be described by the average coupling, whereas zero indicates high impact of dynamical fluctuations and high dynamical variations.

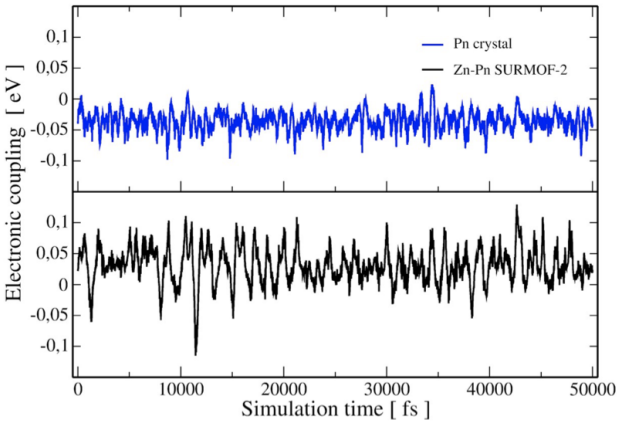

Figure 3.3.: The electronic coupling between PEN molecules in the PEN crystal (in blue) and in Zn-PEN (in black) at 300 K.

The coherence parameter of Zn-PEN is 0.55, which is significantly lower from the coherence parameter for PEN crystal (0.85). This means that the nuclei fluctuations of the PEN in Zn-PEN will affect electronic properties at ambient temperatures more, lowering the efficient charge transfer through the pathways of the highest electronic coupling of the orbitals of the neighboring molecules, i.e. lowering mobility in comparison to the PEN crystal. Among the possible pathways towards enhancing the charge carrier characteristics of Zn-PEN is functionalization of the pristine PEN linkers, enabling suppressing the energy-free dynamical movements of linkers constraining their positioning in the SURMOF film.

3.3.3. Temperature Dependency of the Hole Mobility

Figure 3.4 shows the computed temperature dependence of the mobilities. In agreement with experiment, we find an increase of mobility with temperature, indicating that the transport mechanism is indeed at the transition from Marcus hopping to delocalized band-like transport: as described above, the charge carriers are slightly delocalized, however, we find still activated transport due to the relation of electronic coupling (30 meV) and reorganization energy (93 meV). As expected for activated transport, the mobility decreases for

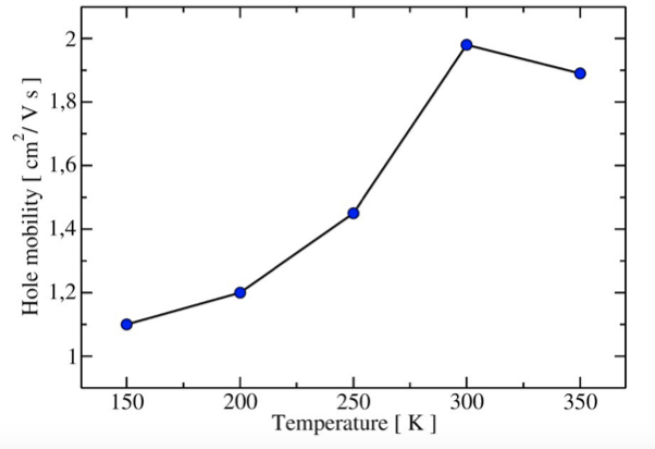

Figure 3.4.: Temperature dependence of the hole mobility in the Zn-PEN obtained using the direct propagation approach.

higher temperatures, which occurs here after 300 K. Theoretically predicted mobilities are slightly higher than experimental values. This discrepancy is related to approximations used in the computational models (however a more accurate match cannot be expected) and considering the mobility in [001] direction, while experimental measurements can be regarded as an average value over the whole material.

3.4. Conclusions

Our theoretical findings have confirmed that the transport mechanism along the 1D PEN stacks is primarily influenced by dynamic contributions. These contributions arise from the rotations of the PEN linkers around the 6,13-axis, which is defined by the two metal-coordinating carboxylate groups. The frustrated rotation leads to fluctuations in the inter-PEN electronic coupling and dynamic disorder. As a result, there is partial delocalization of holes and a charge transport mechanism that lies at the borderline between localized hopping and delocalized charge transport. By conducting detailed static and dynamic quantum-mechanical investigations, we have gained insights into

the fundamental principles that govern the charge carrier properties of such arrays of OSC compounds.

4. Charge Phonon Interaction

4.1. Introduction

For the past four decades, extensive research has been dedicated to organic semiconductors (OSCs) due to their remarkable versatility in organic electronics applications such as light-emitting diodes, photovoltaic cells, and field-effect transistors [46–48]. However, despite their widespread use, a comprehensive understanding of the underlying charge transport properties in OSCs is still elusive. OSCs fall into the intermediate range of charge transport capabilities, which poses a challenge in applying established theories like band theory or small polaron hopping, except within specific temperature conditions. The description of OSC behavior is further complicated by dynamic disorder [74]. Unlike inorganic semiconductors with their relatively static crystal structures, OSCs consist of loosely bound individual molecules, often connected through van der Waals interactions [12]. Even when OSCs exhibit a crystalline structure, this results in significant dynamic disorder, profoundly impacting their charge transport properties. Notably, promising OSCs like rubrene, pentacene, and anthracene exhibit fluctuations in intermolecular electronic couplings on a similar scale to the coupling itself, highlighting the substantial role of dynamic disorder [75]. Rather than viewing dynamic disorder as a mere perturbation, it should be recognized as a fundamental aspect of the experimentally observed charge transport properties in OSCs.

While many studies have acknowledged this phenomenon, Schweicher et al. suggested that only a few distinct modes of motion, termed "killer modes," account for the majority of electronic coupling fluctuations. These killer modes transiently disrupt charge mobility and hold immense potential for advancing OSC design by achieving previously unattainable charge mobilities [76].

In this research we tried to establish a method to deeply investigate these killer modes, and examine the effect of this specific collective motions on the

hole mobility of the anthracene as are test case using the fewest switches surface hopping algorithm to propagate the charge through the material. We aim to gain a profound understanding of killer modes nature and implications in OSCs. Ultimately, understanding of the killer modes may open doors to the development of highly sophisticated OSCs with unprecedented charge mobility.

4.2. Methodology

4.2.1. System Preparation

A supercell of the anthracene was created using its crystallographic input file, composed of 5x30x5 unit cells. The force field parameters were obtained from the general AMBER force field (GAFF) [66], except for the atomic charges, which were calculated using restrained electrostatic potential fitting (RESP) at the HF/6-31(p, d) level of theory using Gaussian16 [72].

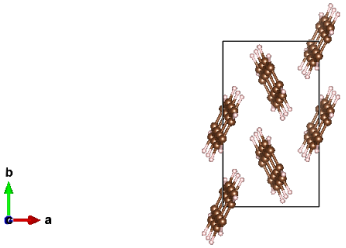

Figure 4.1.: Anthracene crystal structure

4.2.2. Calculation of the Eigenmotions

After energy minimization, the crystal was equilibrated using NVT ensemble at 300 K for 1 ns, utilizing a time-step of 2 fs. The Berendsen thermostat was employed to ensure canonical sampling during equilibration. In order to generate the covariance matrix of the relative motion of the monomers in a

dimer, production simulations were conducted for 20 ns, employing the same settings as the equilibration phase. Covariance matrix which describes the correlation between the motion of different atoms or residues were built up for a dimer coordinate in the b direction of the anthracene crystal, sampled from the resulted MD trajectory. The phonon modes of the dimer in the crystal were obtained from non-mass weighted principal component analysis of the covariance matrix.

4.2.3. Principal Component Analysis

Principal component analysis (PCA) is a widely used method for analyzing trajectories obtained from molecular dynamics (MD) simulations. It allows the decomposition of the motion of a selected part of the system into independent modes of motion known as eigenmodes. In the case of N atoms, these eigenmodes are obtained as eigenvectors of a symmetric $3N \times 3N$ covariance matrix C, whose elements are given by:

$$C = \langle M_{ii}^{1/2}(x_i - \langle x_i \rangle) \cdot M_{jj}^{1/2}(x_j - \langle x_j \rangle) \rangle \tag{4.1}$$

Here, i and j represent the Cartesian coordinates x_i of the atoms being analyzed. The angle brackets $\langle\rangle$ indicate time-averages over the entire simulation. The elements M_{ii} and M_{jj} correspond to the diagonal elements of a $3N \times 3N$ matrix M. If mass-weighted coordinates are desired, M is the atomic mass matrix, otherwise it is an identity matrix for non-mass-weighted coordinates. Mathematically, the decomposition of motion into eigenvectors can be expressed as the diagonalization of covariance matrix C:

$$\mathbf{R}^T C \mathbf{R} = \Lambda \tag{4.2}$$

This equation yields eigenvectors R_i as columns of the orthonormal matrix R and the corresponding eigenvalues $\lambda_i = \Lambda_{ii}$ as entries of the diagonal matrix Λ. The resulting eigenvectors can be interpreted as describing linear displacements from the average structure. Since the eigenvectors are mutually orthogonal, the motion along these displacements can be considered independent modes of motion.

Projection of the displacement vectors of the system from its average structure onto its eigenvectors, $\mathbf{P}(t)$ can be calculated as follows:

$$\mathbf{P}(t) = \mathbf{R}^T \mathbf{M}^{1/2} (\mathbf{x}(t) - \langle \mathbf{x} \rangle) \tag{4.3}$$

These scalar values can be interpreted as a measure of the contribution of the respective eigenvector R_i to the overall displacement from the average structure.

4.2.4. Mode Elimination

The specific modes of motions can be eliminated from the dynamics of the system by applying a restraining harmonic bias on the projection of the trajectory in the direction of the corresponding eigenvectors during the course of MD simulation. This can be achieved using the following equation:

$$V(p) = \sum_i k_i (p(t) - p_{\text{ref}})^2 \tag{4.4}$$

In this equation, the vector $p = (p_1, ..., p_N)$ indicates that multiple eigenmodes can be restrained simultaneously, with individual force constants specified by $k = (k_1, ..., k_N)$ as desired.

In this research all the covariance analysis have performed by GROMACS 2018 [77]. The mode elimination has been implemented using PLUMED software [78] which is coupled with the GROMACS to modify the dynamics of the system on the fly.

4.2.5. Charge Mobility Calculations

In order to investigate the hole transfer in the anthracene under the condition that some eigenmodes of motion are restraint, we have used the fewest switches surface hopping (FSSH) (chapter 2) algorithm implemented in a local version of GROMACS 4.6, where non self-consistent variant of the density functional tight-binding (DFTB) (chapter 2) is also implemented to solve the TDSE. For this aim we equilibrated another simulation box of the anthracene crystal as before. A line of molecules in the b direction containing

28 anthracene molecules have been selected as the QM-zone, where the hole wavefunction is propagated. For each set of calculations we considered 250 separated trajectories to propagate the charge and then the mean square displacement of the charge has been calculated by averaging its values over all the trajectories. The timestep for the evolution of the atomic degrees of freedom which are treated classically was set to 0.10 fs. The TDSE has was solved numerically, in order to propagate the electronic degree of freedom in the QM-zone, using forth order Runge-Kutta algorithm with the integration timestep of 0.01 fs. In order to eliminate the desired modes of motion in the QM-zone, a bias has been set to restraint the projection of the motions along the specific eigenmodes, equation 4.4, already calculated from the PCA analysis of covariance matrix of a dimer in the b direction of the anthracene crystal and applied to every possible dimers in the QM-zone which their monomers are nearest neighbors. The biased constant used to suppress the eigenmodes was set to $5 \times 10^6 kJmol^{-1}nm^{-2}$.

4.3. Results and Discussion

4.3.1. Eigenmodes of the anthracene dimer

Figure 4.2 illustrates the eigenvalues of the eigenvectors of the covariance matrix. As we considered an anthracene dimer in the b crystallographic direction for the covariance analysis, the covariance matrix has 144×144 dimension. Therefor, 144 eigenvectors and corresponding eigenvalues are expected from the diagonalization of the covariance matrix. Since the importance of the eigenvectors decrease rapidly, as it is indicated by the value of eigenvalues, we only presented the first 20 eigenvalue-eigenvectors in the figure 4.2. Based on the figure 4.2 the first five eigenvectors has the most important contribution to describe the relative motion of the dimer, as the value of the eigenvalue of the 6th eigenvector is about 90% off from the first one.

4.3.2. Killer Mode Identification

In order to identify the potential killer modes, we calculated the hole coupling along the first six eigenvectors calculated from the PCA analysis of the

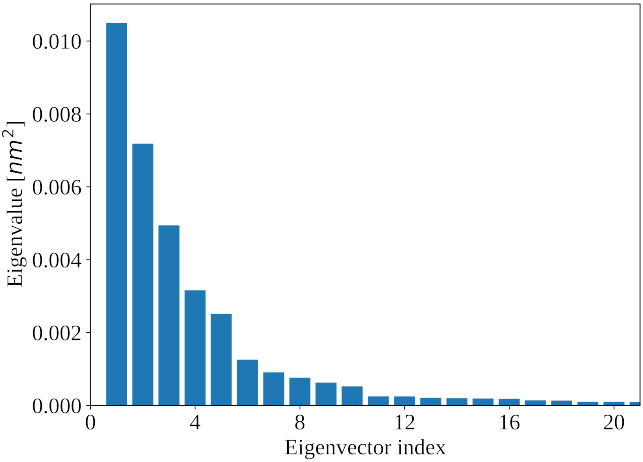

Figure 4.2.: Eigenvalues of the corresponding eigenmodes of the anthracene dimer in the b direction of the crystal, calculated from the diagonalization of the covariance matrix.

covariance matrix figure 4.3. The calculation of the hole coupling has been done using the non self-consistent variant of the density functional tight-binding method (DFTB) as discussed in chapter 2. Trajectories representing the movement associated with each eigenvector were obtained by interpolating linearly between extreme displacements observed in an unrestrained MD simulation. It is worth noting that the magnitudes of the minimum and maximum displacements from the average structure are not equal for individual modes or between different modes due to the trajectory generation method. Nonetheless, it shows in the figure 4.3, that the eigenmode 1 and 3 exhibit the largest deviations in the hole coupling.

The first and third modes are illustrated in the figure 4.4. Therefor, first eigenmode, often referred to as the "long-axis sliding motion" in the literature [76] and commonly observed in oligoacenes and their derivatives, together with third eigenmode were chosen as the target modes for restraint in the subsequent simulations.

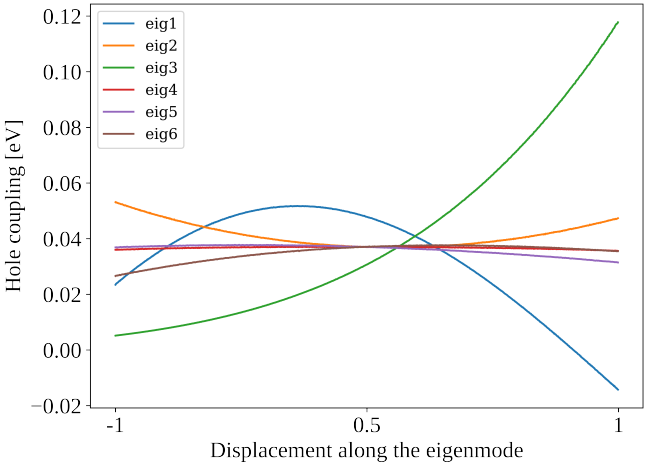

Figure 4.3.: Scanning the hole coupling as a function of displacement along the first six eigenmodes of anthracene dimers in b direction. 1 and -1 correspond to maximum and minimum displacements.

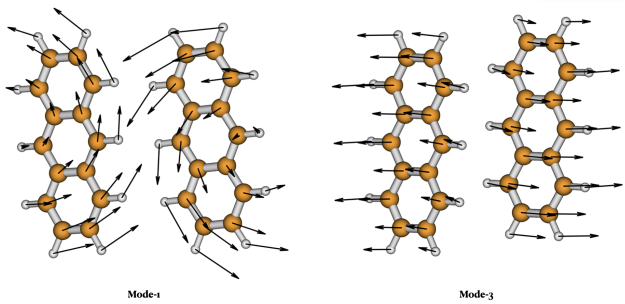

Figure 4.4.: Illustration of the first and third eigenmode of ANT dimer in b direction

4.3.3. The Effect of Killer Mode Elimination on the Hole Coupling

Table 4.1 shows the value of the average hole coupling for the dimer geometries sampled from the NAMD, simulation. The structures were sampled every 1 fs for 100 ps and the value of the hole coupling was calculated using nonself-consistent DFTB. The results show that the hole coupling increases by eliminating the first eigenmode (E.M.) which caused by the fluctuations of the hole coupling along the third eigenmode not being balanced in the absence of the first eigenmode 4.3. The opposite occurs by the elimination of the third mode but this time the fluctuations of the hole coupling along the fist mode is the cause of increment in the average hole coupling 4.3. Elimination of the both eigenmode 1 and 3 which have the main contribution to the fluctuations of the hole coupling in anthracene would leave the average of the hole coupling almost intact, although the standard deviation of the hole coupling is reduced by more than 50%. Based on our assumption, these two specific modes can deteriorate the hole mobility of the anthracene in the b direction by increasing the fluctuations.

Table 4.1.: Average and standard deviation of the hole coupling of an anthracene dimer in the b direction before and after eigenmode (E.M.) elimination. The first row shows the restrained eigenmode.

	unrestrained	1st E.M.	3rd E.M.	1st & 3rd E.M.
$\langle J \rangle$ [eV]	0.042	0.044	0.037	0.039
J_{std} [eV]	0.024	0.021	0.016	0.011

4.3.4. The Effect of Killer Mode Elimination on the Hole Mobility

In order to see the effect of killer modes elimination on the mobility of the hole in the anthracene crystal b direction, the hole wavefunction was propagated using the fewest switch surface hopping algorithm with and without mode elimination. The setup for this part has been explained in section 4.2.5. In our simulation the eigenmodes were calculated once for a dimer coordinate sampled from a long MD simulation, 20 ns, and then used to suppress the motion along the desire modes for every single dimer in the QM-zone where their monomers were nearest neighbors.

Figure 4.5 shows the correlation between the eigenmodes of two different anthracene dimers in the b direction. This figure indicates that the eigenmodes of different dimers of the same kind correlate well specially for the first eigenmodes, where were our main concern. Therefor, employing the eigenmodes of one dimer are applicable for the mode elimination of the other dimers of the same kind if the proper sampling is done.

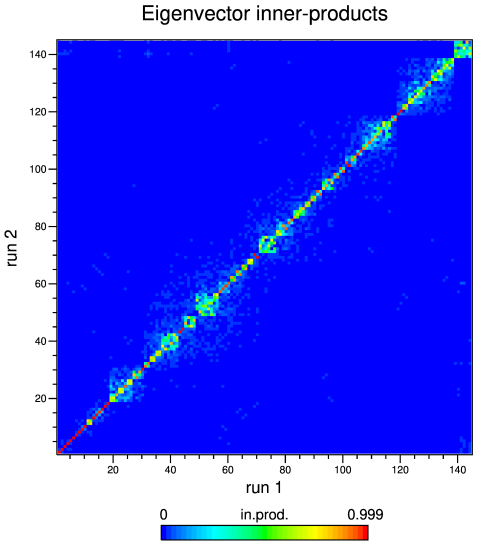

Figure 4.5.: Projections of eigenvectors, extracted from two different dimers in the simulation box, on each other

Table 4.2 shows the results of the NAMD simulation. The hole wavefunction was propagated using FSSH algorithm on a 1D line of anthracene molecules in the b direction. The details of the setup can be found in the preparation section. The results indicate that the value of the charge mobility increases more than two times only by elimination of the first and third eigenmodes. The value of IPR which indicates the number of molecules that the hole wavefunction is delocalized on, is slightly increased by the mode elimination. Therefor, the increment in the mobility could be because of the charge being more delocalized after mode elimination, and also fewer fluctuations of the hole coupling. These results show that the first and third eigenmodes of motions in the anthracene dimer in the b direction can be considered as the

Table 4.2.: NAMD simulation results of the hole propagation in anthracene b direction under the condition where some eigenmodes of motion are restrained. μ is the hole mobility and *IPR* is the inverse participation ratio which shows the degree of the charge delocalization

	unrestrained	1st E.M.	3rd E.M.	1st & 3rd E.M.
$\mu\ [cm^2/V.s]$	2.57	3.19	5.25	6.73
IPR	2.31	2.41	2.50	2.86

killer modes, but this result should be tested by the inclusion of more cases of OSCs in different crystallographic directions which is our consideration to support the current results.

4.4. Conclusions

In conclusion, we have successfully developed a method to constrain specific eigenmodes while preserving the overall system dynamics. Our findings indicate that changes in mean hole couplings, in addition to fluctuations in hole couplings, may play a crucial role in distinguishing killer modes. Importantly, our approach can be readily applied to other oligoacene crystals without requiring anthracene-specific components.

The findings suggest that by removing the first and third eigenmodes, the charge mobility significantly increases by more than two-fold. Additionally, there is a slight increase in the value of the Inverse Participation Ratio (IPR), which indicates a higher degree of molecular delocalization for the hole wavefunction. These results imply that the enhanced mobility can be attributed to both the increased delocalization of the charge after mode elimination and the reduced fluctuations in hole coupling.

To strengthen our conclusions and validate our assumption, we will expand our simulations by considering other oligomers.

5. Exciton Transfer using Machine Learned Hamiltonian

5.1. Introduction

Theoretical approaches employing simulation techniques play a pivotal role by complementing or expediting experimental studies, facilitating efficient screening of a vast chemical space for compounds with promising properties prior to their synthesis. To achieve this, it is imperative to develop fast and robust methods capable of simulating charge and exciton transfer in large molecular systems, while accurately reproducing experimentally observable quantities such as exciton diffusion constant.

Data-driven approaches, such as machine learning (ML) methods, have emerged as valuable tools for predicting charge and exciton transfer properties. In particular, neural network (NN) models have been successfully employed to forecast charge transfer couplings in both organic and metal-organic systems [16–18]. Neural networks have also demonstrated their efficacy in predicting excitation energies in biological systems [19]. Additionally, ML-driven excited-state molecular dynamics have been extensively explored, focusing on small organic molecules [18, 19]. By training ML models on small yet representative datasets, which include relevant electronic parameters obtained from quantum chemistry calculations, it becomes possible to utilize computationally efficient ML models to drive transfer simulations. This offers a significant advantage over costly on-the-fly quantum chemical calculations, which struggle to handle the computational demands associated with large system sizes and lengthy trajectories needed for accurate prediction of the observable.

In this study, we present a multiscale method for the propagation of Frenkel singlet exciton in OSCs using neural network models that predict site energies and excitonic couplings together with their derivatives which are critical

for our non-adiabatic molecular dynamics calculation scheme. We used the fewest switches surface hopping algorithm (FSSH) to propagate the exciton through our systems. Long-range correction version of density functional tight-bonding with self consistence charges (LC-DFTB2) has been used to generate high-quality data required for the networks to be trained. In this work we considered for types of OSCs crystals, Anthrane (ANT), Pentacene (PEN), Perylenediimide (PDI), and Diindenoperylene (DIP) to calculate their exciton diffusion constant using the abovementioned method Figure 5.2.

5.2. Methodology

5.2.1. Frenkel Exciton

Frenkel excitons are a type of excited state that can occur in molecular crystals and organic semiconductors. They are formed when an electron is excited from the ground state to a higher energy level within a molecule, creating a localized electronic excitation known as an exciton. In Frenkel excitons, the electron and the hole are both localized within the same molecule, leading to a strong Coulomb interaction between them.

The Hamiltonian for a Frenkel exciton can be written as

$$\hat{H} = \sum_i \epsilon_i \hat{a}_i^\dagger \hat{a}_i + \sum_{i \neq j} V_{ij} \hat{a}_i^\dagger \hat{a}_j, \tag{5.1}$$

where ϵ_i is the energy of the ith excited state, $\hat{a}_i^\dagger$ and $\hat{a}_i$ are creation and annihilation operators for the ith state, and V_{ij} is the Coulomb interaction between the ith and jth states. The exciton can be described by a wave-function $\Psi(\mathbf{r}_1, \mathbf{r}_2)$, where $\mathbf{r}_1$ and $\mathbf{r}_2$ are the positions of the electron and hole, respectively [79, 80].

The properties of Frenkel excitons are strongly influenced by the molecular structure of the material. This leads to a dependence of exciton energy on intermolecular separation, with exciton energies typically decreasing as the molecules are brought closer together [81].

In addition to their role in molecular crystals and organic semiconductors, Frenkel excitons have also been studied in other systems, such as carbon

nanotubes and graphene. Overall, Frenkel excitons are an important type of excited state in molecular systems, with a wide range of potential applications in areas such as optoelectronics and energy conversion.

5.2.2. Exciton coupling

Coulomb coupling with LC-TD-DFTB

The calculation of the pure Coulomb coupling between transitions from the ground state (g) to the excited state (e), respectively on sites n and m involves the summation of products of the transition charges (Q_{eg}) for atoms A in site m and atoms B in site n. This can be represented as [82]

$$J_{mn}(eg, eg) = \sum_{A\in m}\sum_{B\in n} Q^A_{eg} Q^B_{eg} \gamma_{AB}. \tag{5.2}$$

In DFTB, the second-order Coulomb interaction, represented by γ_{AB} is calculated using a two-electron integral

$$\gamma_{AB} = \int\int \frac{1}{|r-r'|} \frac{\delta^2 E_{xc}[\rho_0]}{\delta\rho(r)\delta\rho r'} F_A(r) F_B(r') dr dr'. \tag{5.3}$$

Neglecting overlap and exchange effects results in a pure Coulomb interaction, which can be expressed as

$$\gamma_{AB} = \int\int \frac{1}{|r-r'|} F_A(r) F_B(r') dr dr', \tag{5.4}$$

where the shape-functions $F_A(r)$ are normalized spherical charge density distributions given by exponential decaying Slater-type orbitals (STOs) used as a basis set for solving the Kohn-Sham (KS) equations [83]

$$F_A(r) = \frac{\tau_A^3}{6\pi} \exp\left(-\tau_A |r - r_A|\right). \tag{5.5}$$

The integral is solved to obtain the expression for γ_{AB}, which depends on the distance between atoms A and B ($R = |r_A - r_B|$) as well as the decay parameter τ_A and τ_B associated with the STOs.

Exciton Coupling from Diabatization

In order to calculate the excitonic coupling between an arbitrary number of states in a molecular dimer we have used a diabatization technique. The procedure is based on finding the diabatic states with a desired property as close as possible to that of some reference states [84].

Considering a dimer system with n adiabatic singlet excited states of interest, with energies $E_{A1}, E_{A2}, \ldots, E_{An}$, the adiabatic (diagonal) Hamiltonian matrix can be expressed as:

$$H_A = \begin{bmatrix} E_{A_1} & 0 & 0 & \ldots & 0 \\ 0 & E_{A_2} & 0 & \ldots & 0 \\ \vdots & \vdots & \vdots & \ddots & \vdots \\ 0 & 0 & 0 & \ldots & E_{A_n} \end{bmatrix} \tag{5.6}$$

Typically, diabatization methods seek to identify the optimal unitary transformation C that can produce diabatic states that closely resemble reference states with well-defined characteristics, such as Frenkel excited states that are localized on a single molecule. It has been shown that the atomic transition charges of each excited state can provide insight into its nature, such as its degree of localization or charge transfer (CT) character [85]. The adiabatic ATC matrix q_A, which contains the atomic transition charges (ATCs) of each interested excited state $(q_{A_1}, q_{A_2}, \ldots, q_{A_n})$ is linked to the diabatic ATC matrix q_D through the unitary matrix C^T.

$$q_A = q_D.C^T \tag{5.7}$$

After obtaining the orthogonal transformation matrix $C = C_{ij}$, the diabatic Hamiltonian H_D can be expressed as $H_D = CH_AC^T$, where C^T denotes the transpose matrix of C. The diagonal elements of H_D correspond to the diabatic energies (E_{D_i}), while the off-diagonal elements correspond to the excitonic couplings (J_{ij}). It is worth noting that the diagonal and off-diagonal elements of H_D for the dimer system can be used to construct an excitonic Hamiltonian for similar molecular clusters that are larger.

By relying on chemical knowledge, we can postulate the existence of an "optimal" diabatic electronic transition charge matrix $(q_{D,ref})$. This matrix

can be derived from the atomic transition charges of certain reference systems. The details about finding the suitable diabatic charge matrix can be found in the reference [84].

The goal is to find the unitary transformation matrix C that minimizes the difference between q_D and $q_{D,ref}$. This can be achieved using the following equation:

$$C^T = argmin_R||q_A R - q_{D,ref}|| \tag{5.8}$$

Here, $||\cdot||$ represents the Frobenius norm, which is the square root of the sum of the squares of all matrix elements. The matrices q_A and $q_{D,ref}$ are rectangular matrices, where the number of columns equals the number of states of interest, and the number of rows is much larger, corresponding to the total number of atoms in the system.

Equation 5.8 has a unique solution as follows [86]:

$$C^T = UV^T \tag{5.9}$$

Here, U and V^T are the matrices obtained through the singular value decomposition (SVD) [87] of the matrix $M = (q_A)^T q_{D,ref} = U\Sigma V^T$.

Similar to other diabatization methods, this approach is able to capture the relevant physics of short-range contributions, including exchange, overlap, and charge-transfer mediated terms, although considering the short-range contributions are beyond the scope of this research.

5.2.3. Exciton Reorganization Energy

The reorganization energies related to excitons, which are denoted as λ, are commonly divided into two contributions, the "inner-sphere" and "outer-sphere". As the outer-sphere reorganization energy is negligible for the OSCs, we only consider the inter-sphere contributions. The inner-sphere contribution is calculated using the four-point scheme [13] for a molecule in the gas phase via equation 5.10

$$\lambda = \lambda_0 + \lambda_1,$$

$$\lambda = [E_{S_1}(Q_{S_0}) + E_{S_0}(Q_{S_1})] - [E_{S_1}(Q_{S_1}) + E_{S_0}(Q_{S_0})], \tag{5.10}$$

where E_{S_0} and E_{S_1} denote the potential energy of the ground state and first excited state, respectively, and Q_{S_0} and Q_{S_1} represent the nuclear coordinates at the respective potential energy minima Figure. 5.1.

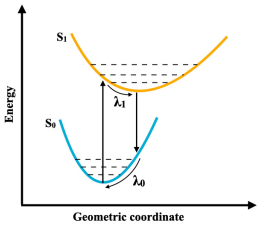

Figure 5.1.: Schematic of the reorganization energy (relaxation energy) in the singlet excitonic system. S_0 and S_1 represent the ground and first excited PES of the system.

5.2.4. Neural Networks (NN)

Neural networks are highly versatile statistical models widely used for addressing complex regression or classification problems. They consist of interconnected layers of neurons that process input data. Each neuron performs a linear combination of the inputs, incorporating adjustable weights. These linear combinations are then passed through non-linear activation functions, enabling the network to approximate intricate functions accurately.

During the training process, the network's weights are initialized randomly and iteratively adjusted to minimize the discrepancy between predicted and

reference values, as measured by a cost function. The popular backpropagation algorithm plays a vital role in this optimization process by computing derivatives of the cost function with respect to the weights.

The architecture of a neural network, including the number of layers and neurons, plays a crucial role in its performance. These design choices, known as hyperparameters, are not optimized automatically during training. Instead, a dedicated hyperparameter optimization process is employed, which typically involves training the network multiple times on the same dataset while varying the hyperparameter values.

Previous studies have utilized simple fully-connected networks with a nonlinear activation to forecast site or excitation energies, as well as couplings [88, 89]. Recently, Li et al. have introduced a NN architecture designed explicitly for photo-dynamics simulations of organic molecules, which is implemented using Tensorflow and is available in the pyNNsMD package [90]. This architecture can predict energies and gradients of multiple electronic states and features a straightforward representation that is integrated into the model. It is well-suited for the problem at hand and serves as the foundation for the models in this research.

5.2.5. System Preparation

Training Data Sampling

In order to generate the training data required for our NN model fitting, the simulation box of each OSC was created based on the expansion of its unitcell in different crystallographic directions. Figure 5.2.

The force field parameters were obtained from the general AMBER force field (GAFF) [66, 67] and atomic charges were calculated by restrained electrostatic potential fitting procedure (RESP) [68, 69] with HF/6-31G* [70, 71] level of theory using Gaussian 16 software [72]. After energy minimization the initial structures were equilibrated for 1 ns at 500K in the NVT ensemble using Nose-Hoover thermostat [73]. The temperature was chosen high enough to increase the chance of the covering of the possible conformational space. QM/MM was performed after the equilibration step for 100 ps to generate the LCDFTB ground and excited state geometries. The coordinate of monomer

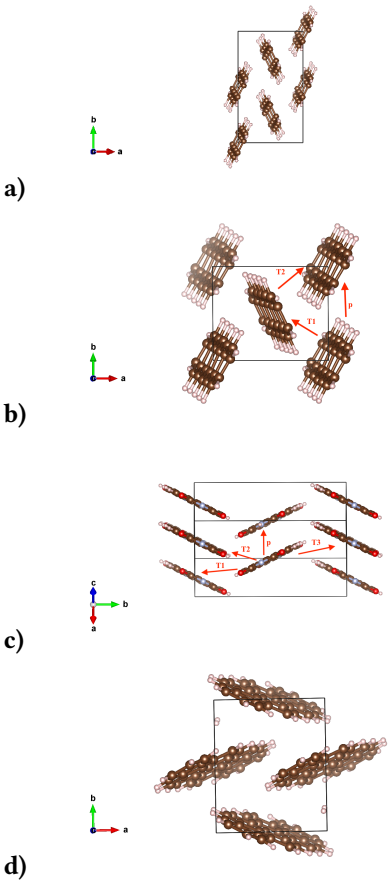

Figure 5.2.: Illustration of the of a) ANT, b) PEN, c) PDI, and d) DIP crystals.

and dimer from different part of the crystals were sampled every 100 fs. Gromacs 5.0.4 was used to perform molecular dynamics simulation.

Propagation

In order to simulate the exciton transfer using the fewest switches surface hopping algorithm implemented into the local version of GROMACS 4.6, separate crystals of ANT, PEN, PDI, and DIP were created based on their experimental measured unitcells. The QM zones were chosen as one-dimensional lines of molecules along the respective directions in the middle of each crystal containing enough number of molecules. After equilibration at 300 K, initial structures of the crystals were sampled every 10 ps for the subsequent simulations of exciton transfer. The exciton wavefunction was initially localized on the first molecule. We used a time step of 0.100 fs for the propagation of nuclei, the TDSE was integrated numerically with the fourth-order Runge-Kutta algorithm with an integration time step of 0.010 fs. Mean squared displacement (MSD) were calculated from its average value over 600 trajectories, which were simulated for 1 ps each.

The diffusion constant of the exciton was calculated from the MSD according to the following equation:

$$\begin{aligned} D &= \frac{1}{2n} \lim_{t\to\infty} \frac{dMSD(t)}{dt}. \\ MSD(t) &= \frac{1}{N_{traj}} \sum_{l}^{N_{traj}} \sum_{A} (x_A(t)^{(l)} - x_0^{(l)})^2 P_A(t)^{(l)}. \end{aligned} \tag{5.11}$$

n is the dimensionality which is set to one in our calculations. $x_A(t)^{(l)}$ and $P_A(t)^{(l)}$ are the center of mass of molecule A and the corresponding diabatic population along the trajectory l, respectively. $x_0^{(l)}$ is the center of exciton at $t = 0$.

5.3. Results and Discussion

5.3.1. Site Energy

In order to identify the relevant on-site singlet excitations contributing to the Frenkel states, single molecule coordinate of the ANT, PEN, PDI, and

DIP are taken from the crystal structure and after geometry optimization using LC-DFTB2, the vertical electronic transition energies are calculated via TD-LC-DFTB2. The range-separation parameter ω is set to $\omega = 0.3/a_0$ for the computation of the electronic parameters, which was already calculated in reference [91]. As it is shown in the Table 5.1, oscillator strengths and excitation energies of the single molecules in the gas phase calculated by TD-LC-DFTB2 are in close relation with the corresponding TD-DFT calculations using range-separated functionals CAM-B3LYP and ωB97xd, which has been shown to provide an accurate description of valence and charge-transfer excitations [92]. The maximum relative error, σ of the first excitation energy belongs to ANT which is under 10 present. The results are also depicted in Figure 5.3 and 5.4. More inclusive benchmark of the excitation energy calculation using TD-LC-DFTB2 can be found in the references [23–25].

Table 5.1.: Comparison of the vertical excitation energy [eV] and oscillator strength calculated by TD-LC-DFTB2 and TD-DFT using long range separated functionals ωB97xd and CAM-B3LYP with 6-31G(p, d) level of theory. σ is the relative error of the vertical transition energy calculated by TD-LC-DFTB2 with respect to its value calculated by ωB97xd in [eV].

		CAM-B3LYP	ωB97xd	LC_DFTB2	σ%
ANT	S_1	3.661	3.685	3.374	8.5
	f	0.088	0.090	0.090	
	S_2	4.180	4.160	3.898	
PEN	S_1	2.355	2.416	2.322	4.0
	f	0.075	0.081	0.090	
	S_2	3.492	3.525	3.276	
PDI	S_1	2.845	2.877	2.715	5.4
	f	0.765	0.771	0.681	
	S_2	3.771	3.796	3.209	
DIP	S_1	2.794	2.831	2.623	7.2
	f	0.954	0.966	0.906	
	S_2	2.978	3.053	2.768	

Singlet transition with the lowest energy (S_1) and non-zero oscillator strength f are considered as excitation contributing to the Frenkel states. It is worth to note that, our calculation using TD-LC-DFTB2 indicates that the first transition (S_1) in all the considered material in this research are completely dominated by HOMO to LUMO transition. Moreover, the second-lowest

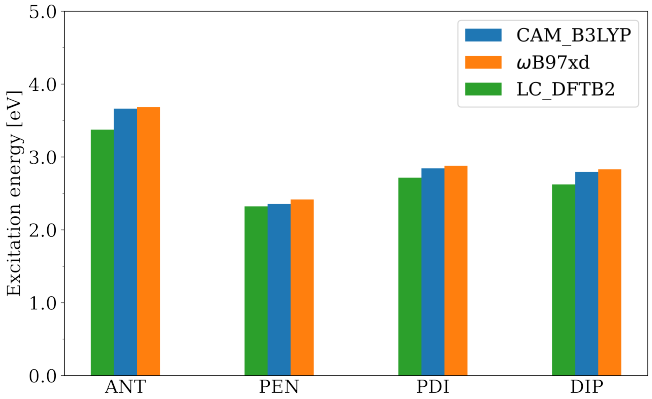

Figure 5.3.: Comparison of the vertical excitation energy of S_1 [eV] calculated by TD-LC-DFTB2 and TD-DFT using long range separated functionals ωB97xd and CAM-B3LYP with 6-31G(p, d) level of theory.

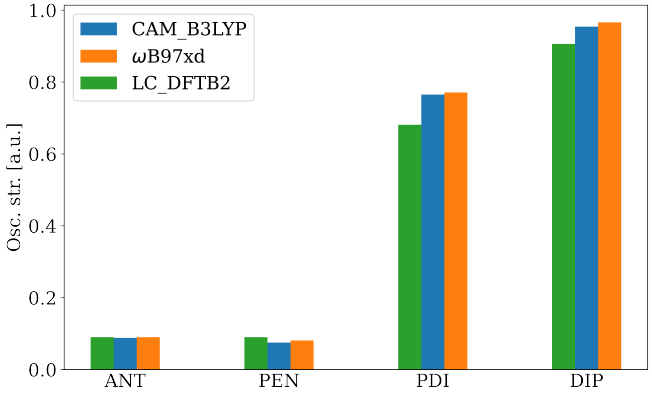

Figure 5.4.: Comparison of the oscillator strength of S_1 calculated by TD-LC-DFTB2 and TD-DFT using long range separated functionals ωB97xd and CAM-B3LYP with 6-31G(p, d) level of theory.

singlet excited state, (S_2), in all cases, but DIP is far enough from the first excited state energetically. The oscillator strength of the second transition, (S_2), in DIP is zero, which makes it a dark state. Therefor, only first singlet excited state (S_1) of the isolated molecules in the gas phase is considered to

be involved in the Frenkel Hamiltonian. The data shown in the table 5.1 are illustrated in the Figure 5.3 and Figure 5.4.

The fact that the low-energy tail of the band created by the crystal intermolecular excitation can be accurately explained by a mixture of the intramolecular S_1 states, and that these states can be approximated as HOMO-LUMO transitions, provides further evidence supporting the credibility of the Frenkel exciton model for the studied cases.

5.3.2. Exciton Coupling

In order to validate the Coulomb coupling calculated by TD-LC-DFTB2, we performed a benchmark against the long range DFT functionals ωB97xd and CAM-B3LYP. For this aim, 1000 dimer coordinates were sampled every 1 ps during 1 ns course of molecular dynamic simulation of each crystal using GAFF force field. The simulation boxes were equilibrated in NVT ensemble using the Nose-Hoover thermostat for 1 ns after energy minimization. The Coulomb coupling for each dimer was calculated using the method described in the section 5.2.2 via TD-LC-DFTB2 and also TD-DFT using ωB97xd and CAM-B3LYP functionals with 6-31G(p, d) basis set. It should be mentioned that only (a) direction in ANT and DIP and (p) direction in PEN and PDI have been considered in this test.

As it is shown in the Figure 5.5, the TD-LC-DFTB2 Coulomb coupling correlates very well with the TD-DFT results as the R^2 value of the corresponding plots are quite close to 1. This is a fascinating observation which makes the TD-LC-DFTB2 an excellent candidate for the investigation of charge and exciton behavior in organic semiconductors, as it is an order of magnitude faster than the DFT counterpart.

In addition to the Coulomb coupling, the performance of TD-LC-DFTB2 in the context of the diabatization scheme explained in the section 5.2.2 has also been tested against TD-DFT, in order to capture the locally excited contribution of the excitonic coupling in the studied crystal in this research.

For this aim, the atomic transition charges (ATC) of the reference diabatic states $q_{D,ref}$, defined as the ATC of the singlet excited state on one isolated monomer in the dimer while the ATC of the other monomer is set to zero. On the other hand, calculation of the singlet excited states on dimers allowed to obtain the ATC q_A and the energies E_A of the adiabatic states.

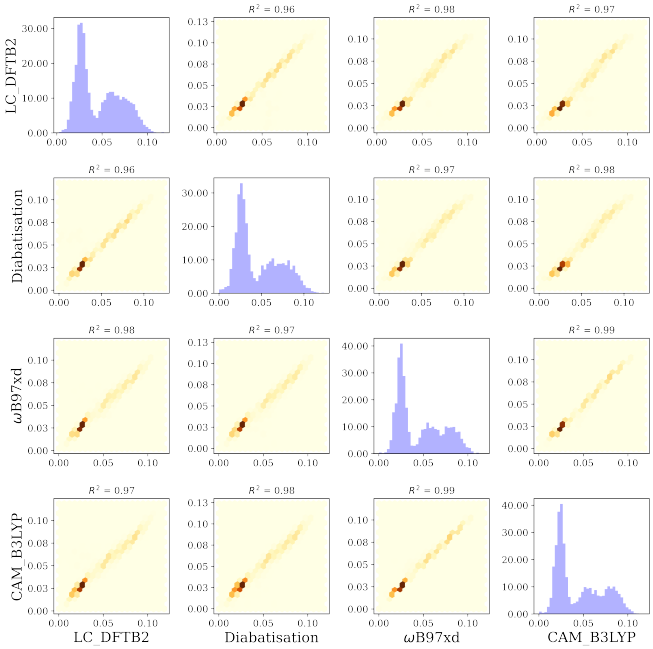

Figure 5.5.: Coulomb coupling correlation plots of the ANT, PEN, PDI, and DIP. The unit of the coupling values are eV

In order to identify the number of states required for the diabatization to obtain converged value of the exciton coupling for each case of study, the value of exciton coupling has been calculated as the number of included states in the diabatization increased. According to the Figure 5.6, only 2 singlet excited state is enough to estimate the exciton coupling in ANT, PEN, and DIP while there would be 8 state required to be considered to get the convergence in the PDI case.

5.3.3. Internal Exciton Relaxation

Exciton-phonon coupling and molecular relaxation in the excited state are essential phenomena affecting the energy transport in organic semiconductors. Based on Markus theory the internal relaxation energy plays a vital role in

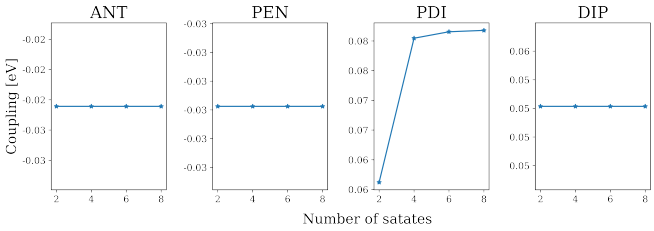

Figure 5.6.: Locally excited contribution of the excitonic coupling calculated via diabatization technique using TD-LC-DFTB2 for ANT, PEN, PDI, and DIP.

the transport efficiency as the diffusion constant is related to it exponentially (chapter 2). The high value of relaxation energies can cause the transport to become incoherent [22].

In table 5.2, we compared the reorganization energy of a single molecule in the gas phase calculated by TD-LC-DFTB2 with DFT results. It is shown that the TD-LC-DFTB2 reorganization energy is close to the result of the long range functionals. The value of the relative error for each case reported in the table indicates that the TD-LC-DFTB2 can predict the value of the internal exciton reorganization energy to relatively good extend. a comprehensive benchmark could be find in the reference [25].

The large value of the reorganization energy in the studied excitonic system indicates a significant difference in the wavefunction of the S_0 and S_1 states.

Table 5.2.: Reorganization energy [meV] calculated from LC-DFTB2 and DFT using range separated fuctionals with 6-31G(p, d) level of theory, σ is the value of the relative error.

	LC_DFTB2	ωB97xd	CAM_B3LYP	σ%
ANT	494	533	533	7.3
PEN	329	388	383	14.1
PDI	367	396	382	3.9
DIP	378	406	390	3.1

5.3.4. Training Data

According to the Frenkel exciton definition, equation 5.1, the site energy of the singlet exciton, ϵ .is defined as the excitation energy of the individual fragments of the crystal. Therefore, 20000 monomer geometries from ground state and excited state QM/LC-DFTB2/MD with 1:1 ratio were sampled based on the procedure explained in the section 5.2.5. Figure 5.7 shows the distribution of the site energy calculated by TD-LC-DFTB2 for each crystal.

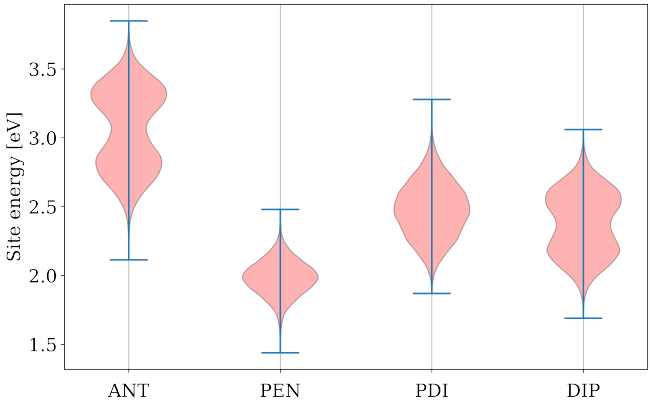

Figure 5.7.: Distribution of the site energy training data of the ANT. PEN, PDI, and DIP

As the behavior of atomic nuclei are described using classical mechanics in our approach, the classical force field potential, V_{FF}, is responsible for the ground state forces acting on the atoms and the difference in atomic forces between the ground and excited states is represented by the negative derivative of the excitation energy, or F_{QM}.

$$m_i \partial_t^2 R_i = -\nabla_i V_{FF} + F_{QM} \tag{5.12}$$

Therefore, in addition to the site energy, its derivative F_{QM} were also included in the training data for each geometry.

In order to generate the training data for the exciton coupling V_{ij}, 20000 dimer geometries were sampled from QM/LC-DFTB2/MM ground and excited state

with 1:1 ratio for each OSC where only one monomer was in the QM zone and the other one was under the classical force field (GAFF).

Few approximations have been taken into account in order for the calculation of the exciton coupling in this research. First, it has been assumed that the short-range contributions of the exciton coupling of the investigated materials are negligible, and the total exciton coupling can be expressed via Coulomb coupling. Figure 5.8 shows the total and Coulomb coupling of a dimer in each OSC crystal structure during a course of MD simulation for 1 ns. According to this result, considering the Coulomb coupling as the dominant contribution of the exciton coupling is a reasonable approximation as the difference between total and Coulomb coupling in Figure 5.8 is negligible for all cases.

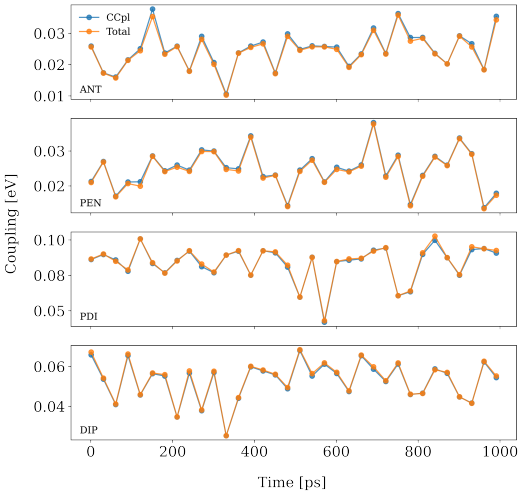

Figure 5.8.: Total exciton coupling vs. Coulomb coupling (Ccpl) for ANT, PEN, PDI, and DIP during a course of MD simulation for 1 ns.

As the second approximation, we assumed that the atomic transition charges (ATC) would not change drastically during the MD simulation. In this case, the ATC of a monomer in the crystal structure could be used for the calculation of the Coulomb coupling of all different instances generated during a course of MD simulation. As Mullikan transition charges has been used for this calculation, the resulted coupling will be called TrMull coupling.

Figure 5.9 shows the comparison between the distribution of the TrMull and the Coulomb coupling for the same set of geometries sampled from the MD simulation of the investigated crystals. According to the Figure 5.9 the mean value of the calculated TrMull and the Coulomb coupling for all the cases are quite close which indicates that taking TrMull coupling instead of Coulomb coupling would be a reasonable approximation.

Using TrMull coupling has two advantages for us. First, the time of calculation is reduced as the ATC is calculated one time and would be used during the entire simulation. Second, by taking the ATC as constant, γAB in equation would only depend on R which enables us to obtain the derivative of the coupling analytically in order to calculate the non-adiabatic vector equation 2.36. The standard deviation of the TrMull couplings are less than the standard deviation of the Coulomb coupling which is a trivial consequence of subtracting the fluctuation of ATC from the calculation.

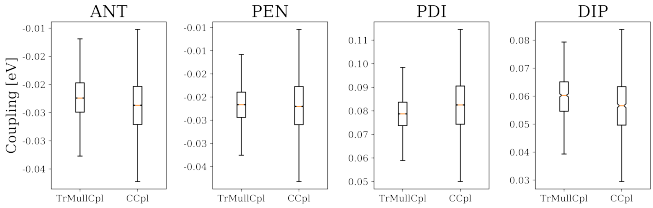

Figure 5.9.: TrMullCpl vs. Ccpl distribution for the MD sampled structures of the ANT, PEN, PDI, and DIP, calculated by TD-LC-DFTB2.

The distribution of the TrMull coupling of the dimers sampled from different crystallographic directions of the studied crystals in this research are shown in Figure 5.10. The derivative of the couplings were also included in each set.

5.3.5. Neural Network Fitting

In this research we used three separate neural network models for the propagation of the exciton using our trajectory surface hopping algorithm. One takes the monomer structure and given the corresponding first singlet excitation energies together with their gradients calculated by TD-LC-DFTB2, the

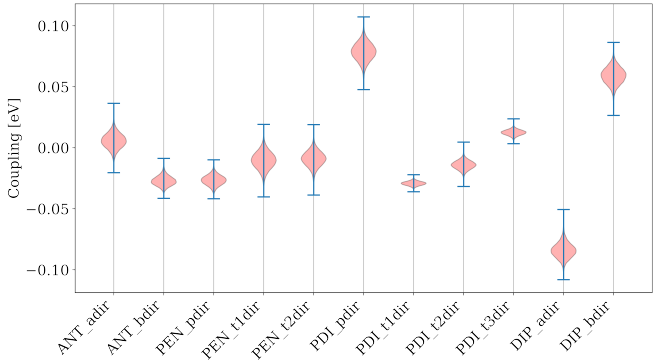

Figure 5.10.: Distribution of the TrMull coupling training data of the ANT. PEN, PDI, and DIP

excitonic site energies and relaxation energies would be predicted. The second model takes dimer structures along with the respective Trmull coupling from TD-LC-DFTB2 and its derivative with respect to atomic coordinates, and predicts the exciton coupling together with the non-adiabatic vector couplings NACVs. The third neural network model would take the monomer coordinates and given the difference between the GAFF forces and the ground state LC-DFTB2, adjusts the forces in a way that reproduces the LC-DFTB2 reorganization energy for each case.

Optimally, the model should require only the coordinates of the fragments/pairs and return the predicted couplings and gradients. We used inverse distance representation to introduce the structures to the neural networks. As the gradients obtained from the model will be converted to forces applied to the system, it is especially important for force predictions to be as reliable as possible. Due to the feedback of the forces to the geometries, a bad force prediction can push the atoms into conformations which are out of the area of the PES sampled during training.

In this work we used the simple fully-connected of the neural network architecture specifically for photodynamics simulations of organic molecules recently presented by Li et al.[132]. This model allows predicting energies and gradients of multiple electronic states, using a simple representation whose calculation is integrated into the model, and is implemented using Tensorflow. This model is implemented into our local version of GROMACS 4.6. We used Softmax activation function to capture the nonlinearity of the

problem we are dealing with in this work. Hyper parameter optimization are done for every single neural network model in this study using Hyperband algorithm [93]. The result of the neural network model fitting are shown in Tables 5.3, 5.4, and 5.5.

Table 5.3.: Neural network models for the TrMull coupling together with the gradients in x, y, and z direction of ANT, PEN, PDI, and DIP in different crystallographic directions. MEA mad Max err. are in [eV].

	R^2	MEA	Max err.		R^2	MEA	Max err.
ANT-adir	0.99	0.009	0.117	ANT-bdir	0.99	0.003	0.045
∂_x	0.99	0.004	0.368	∂_x	0.99	0.003	0.045
∂_y	0.99	0.004	0.436	∂_y	0.99	0.003	0.045
∂_z	0.99	0.004	0.141	∂_z	0.99	0.003	0.045
PEN-pdir	0.99	0.005	0.065	PEN-t1dir	0.99	0.009	0.098
∂_x	0.99	0.003	0.124	∂_x	0.98	0.008	0.279
∂_y	0.99	0.003	0.148	∂_y	0.98	0.008	0.217
∂_z	0.99	0.003	0.105	∂_z	0.95	0.008	0.223
PEN-t2dir	0.99	0.006	0.111	PDI-pdir	0.96	0.032	0.093
∂_x	0.99	0.004	0.366	∂_x	0.99	0.006	0.094
∂_y	0.99	0.004	0.323	∂_y	0.98	0.005	0.086
∂_z	0.99	0.004	0.154	∂_z	0.99	0.006	0.106
PDI-t1dir	0.98	0.004	0.075	PDI-t2dir	0.98	0.010	0.078
∂_x	0.98	0.003	0.074	∂_x	0.95	0.005	0.156
∂_y	0.96	0.002	0.048	∂_y	0.98	0.005	0.208
∂_z	0.97	0.002	0.057	∂_z	0.93	0.005	0.132
PDI-t3dir	0.99	0.004	0.027	DIP-bdir	0.99	0.013	0.157
∂_x	0.99	0.002	0.093	∂_x	0.98	0.004	0.142
∂_y	0.97	0.002	0.114	∂_y	0.82	0.006	0.174
∂_z	0.95	0.002	0.045	∂_z	0.99	0.004	0.161

Table 5.4.: Neural network models for the site energies together with the gradients in x, y, and z direction of ANT, PEN, PDI, and DIP. MEA mad Max err. are in [eV].

	R^2	MEA	Max err.		R^2	MEA	Max err.
ANT	0.99	0.416	3.094	PEN	0.99	0.136	1.054
∂_x	0.99	0.853	18.564	∂_x	0.99	0.301	8.222
∂_y	0.99	0.868	18.803	∂_y	0.99	0.221	4.922
∂_z	0.99	1.036	20.559	∂_z	0.99	0.396	8.581
PDI	0.99	0.288	1.626	DIP	0.99	0.384	3.797
∂_x	0.99	0.492	34.783	∂_x	0.99	1.168	43.229
∂_y	0.99	0.583	46.986	∂_y	0.97	0.837	23.661
∂_z	0.99	0.526	46.587	∂_z	0.99	1.421	50.676

Table 5.5.: Neural network models for the force field correction in ANT, PEN, PDI, and DIP. MEA mad Max err. are in [eV].

	R^2	MEA	Max err.		R^2	MEA	Max err.
ANT				PEN			
ΔF_x	0.97	4.945	91.402	ΔF_x	0.97	9.631	153.400
ΔF_y	0.98	6.832	130.509	ΔF_y	0.96	5.583	71.583
ΔF_z	0.97	7.336	94.262	ΔF_z	0.97	10.111	158.374
PDI				DIP			
ΔF_x	0.98	6.139	1856.788	ΔF_x	0.97	0.147	126.699
ΔF_y	0.97	7.047	337.123	ΔF_y	0.97	4.934	88.226
ΔF_z	0.98	6.268	1435.629	ΔF_z	0.97	9.212	343.554

5.3.6. Exciton Propagation and neural network model validation

In order to investigate the exciton transfer in the studied crystals, we only considered the first neighbor interactions of each direction to train the neural net models and propagated the excitoninc wave function in one dimension. Our investigation on the molecular distance dependency of the TD-LC-DFTB2

Coulomb coupling shows that it drops very fast as the intermolecular distance increases Figure 5.11. For all the studied cases in this research, the Coulomb coupling gets close to zero as the intermolecular distance gets as two times as big as the equilibrium distance of the molecules in the crystal. This fact indicates that it would be sufficient to only take the first nearest neighbor into consideration for our calculation of the exciton diffusion constant in these crystals.

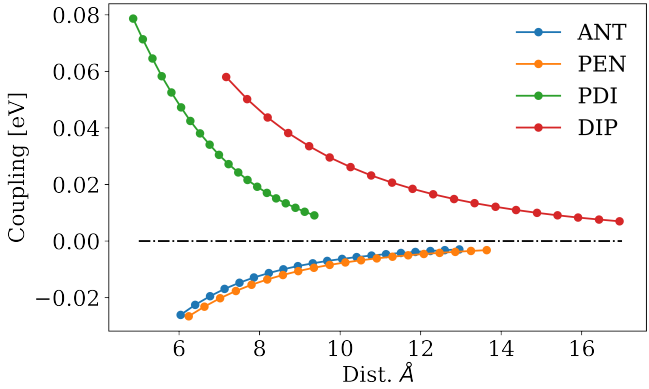

Figure 5.11.: Coulomb coupling calculated by TD-LC-DFTB2 vs. intermolecular distance.

Table 5.6 presents a comparison between the neural network models and the LC-DFTB2 results for exciton coupling prediction. The results show that the neural network models are able to predict the coupling values with a high degree of accuracy across all cases. Moreover, the reorganization energy, which is a critical parameter for the propagation of the wave function, can also be predicted very well by our neural network models. It is worth noting that the excitonic reorganization energy is obtained from the difference between S_0->S_1 and S_1->S_0 transition energies. Therefore, the good agreement between the predicted reorganization energy by the neural network and the LC-DFTB2 results also implies a high level of agreement between the predicted site energies by the neural network and the LC-DFTB2 method.

Excitonic couplings generally exhibit small fluctuations. This can be attributed to the fact that excitonic couplings are only moderately affected by changes in geometry induced by lattice vibrations, given their Coulombic and long-range nature r^{-3}. In the hopping regime (characterized by large barriers), coupling

fluctuations are beneficial for the localized exciton to overcome the activation barrier.

Table 5.6.: Exciton coupling and reorganization energy [meV] of ANT, PEN, PDI, and DIP in different crystallographic directions. ⟨ ⟩ indicates the average values of the properties during a course of MD simulation.

	Dir	Dist	$\langle V^{Coulomb}_{TD-LCDFTB2} \rangle$	$\langle V^{TrMull}_{NN} \rangle$	$\langle \lambda_{NN} \rangle$	$\lambda_{TD-LCDFTB2}$
ANT	a	5.24	6 ± 8	6 ± 6	493	494
	b	6.04	-27 ± 5	-27 ± 4		
PEN	p	6.24	-27 ± 6	-27 ± 4	330	329
	t1	4.69	-10 ± 7	-10 ± 6		
	t2	5.16	-9 ± 7	-9 ± 6		
PDI	p	4.86	82 ± 12	79 ± 7	352	356
	t1	9.40	-32 ± 3	-29 ± 2		
	t2	11.60	-15 ± 6	-14 ± 3		
	t3	15.10	14 ± 4	12 ± 2		
DIP	a	5.58	-85 ± 7	-84 ± 6	378	369
	b	7.17	59 ± 9	59 ± 7		

The distribution of the NN predicted values of the site energies together with the corresponding reorganization eneries and also the predicted value of the coupling in each direction is show in Figure

5.3.7. Exciton Propagation using Trajectory Surface Hopping

The averaged mean-squared displacement (MSD) of the exciton wavefunction, obtained from 600 trajectories for each system, is illustrated in appendix A. The graphs exhibit an initial rapid increase in MSD at short times, followed by an approximately linear increase at longer times. This rapid increase primarily arises from the electronic relaxation of the initially fully localized exciton. However, after the initial relaxation, the populations of the excitonic band states ultimately reach the Boltzmann populations, irrespective of the starting point. As a result, the long-time diffusive dynamics remain consistent regardless of the initial states.

The diffusion constant of the exciton is calculated from the linear portion of the MSD plot, diffusion equation 5.11. Diffusion constants along different

crystallographic directions for the investigated OSCs, are reported in Table 5.6.

The computed diffusion constant magnitudes are in good agreement with existing experimental data. Unfortunately the experimental data is only available for ANT. According to Table 5.7, the diffusion constant value for ANT in the b-direction is 2.1 cm^2s^{-1}. This value is approximately half the experimental measurement and closely matches the calculated value reported in reference [13].

It is worth noting that the diffusion constants obtained from our simulations slightly underestimate the experimental values. This discrepancy can be attributed to a couple of possible reasons. Firstly, our simulations do not account for nuclear tunneling effects, which can become significant when dealing with large activation barriers in the excitation energy transfer process, as seen in the case of ANT. Another potential factor could be the absence of mixing between Frenkel exciton and charge-transfer states in our current simulations, which could enhance singlet exciton diffusion due to the larger exciton dispersion.

High value of the reorganization energy in compare with the value of the excitonic coupling can cause a lower diffusion constant in excitonic systems as it is obvious in the ANT adir and PEN t1 and t2dir. Also in ANT bdir and PEN pdir where, the intermolecular distance and excitonic coupling is comparable, the calculated diffusion constant is more than two times as high as the diffusion constant in ANT bdir, as the value of the reorganization energy in PEN is much lower than its value in ANT bdir.

It has been shown that, considering only the nearest neighbor exciton coupling can enhance the exciton diffusion constant in some cases like PDI and DIP where the second neighbor coupling is not completely vanished [13]. This is because of the long-range nature of excitonic coupling, increasing the localization of excitonic states at the bottom of the excitonic band. Therefore, considering more than the first neighbor coupling can decrease the diffusion constant in these systems.

The value of the diffusion constant for the PDI and DIP could be even lower as the charge transfer states are noticeable in these cases. It has been shown that, the charge transfer states in these systems act as a trap for the charge carrier and therefore decrease the value of the diffusion constant. Including charge transfer states in the Hamiltonian was not in the scope of this research.

The ratio of relaxation energy to excitonic coupling, λ/J, for all the cases investigated in this research is quite large, which predicts incoherent transport. This fact is also consistent with the value of the inverse participation ratio (IPR) which indicates the degree of the excitonic wavefunction delocalization. The value of the IPR for all the cases is 1 except for the PDI pdir and DIP bdir which means the mechanism of the exciton transfer in most of the cases fall in the hopping regime.

The diffusion constant calculated via imlicit relaxation Boltzmann correction fewest switches surface hopping (IR-BC-FSSH) is overestimated in comparison with FSSH in all cases which is consistent with our previous work results for the charge transfer [14]. We used the reorganization energy calculated by TD-LC-DFTB2 for all the IR-BC-FSSH simulations. As the value of the diffusion constant in the studied molecules are too low and the exciton wavefunction is very localized (based on the IPR value), the effect of reorganization energy becomes important for the relaxation of the system.

Table 5.7.: Diffusion constant in $cm^2/s \times 10^{-3}$ and IPR value for the ANT, PEN, PDI, and DIP in different crystallographic directions

		FSSH		IR-BC-FSSH		Ref.
Sys.	Dir.	Diff. const.	IPR	Diff. const.	IPR	Diff. const. [13, 22]
ANT	adir	0.10	1.00	0.40	1.00	0.55
	bdir	2.19	1.03	8.16	1.05	3.3, 5.00
PEN	pdir	7.68	1.08	25.20	1.12	-
	t1dir	0.38	1.01	1.12	1.03	-
	t2dir	0.40	1.01	1.12	1.03	-
PDI	pdir	73.28	1.72	144.51	1.67	26.00
	t1dir	5.85	1.10	17.5	1.10	-
	t2dir	3.36	1.03	7.74	1.03	-
	t3dir	3.89	1.02	3.30	1.02	-
DIP	bdir	80.62	1.41	-	-	-

5.4. Conclusions

In this study, we have developed a multiscale method for simulating the propagation of Frenkel singlet excitons in organic semiconductor crystals (OSCs). Our approach utilizes neural network models to accurately predict site energies, excitonic couplings, and their derivatives, which are crucial for our non-adiabatic molecular dynamics simulation scheme. We employed the fewest switches surface hopping (FSSH) algorithm to simulate the exciton dynamics within the OSCs.

To generate the necessary high-quality data for training the neural networks, we employed the long-range correction version of time dependent density functional tight-binding with self-consistent charges (TD-LC-DFTB2) method. We have shown that the site energy, Coulomb coupling and reorganization energy calculated using TD-LC-DFTB2 are in agreement with the corresponding values calculated by long range TD-DFT.

We applied our method to four types of OSC crystals: Anthrane (ANT), Pentacene (PEN), Perylenediimide (PDI), and Diindenoperylene (DIP). By employing this approach, we calculated the exciton diffusion constant for these OSCs, which is close to the experimental values and other theoretical studies.

This work demonstrates the effectiveness of our multiscale method in accurately simulating exciton propagation in OSCs. The combination of neural network models and the FSSH algorithm provides valuable insights into exciton dynamics and diffusion within these materials. These findings contribute to a deeper understanding of the optical and electronic properties of OSCs, opening doors for the design and optimization of novel materials for organic electronic devices.

6. Summary and Outlook

The investigation of charge and exciton transfer in organic semiconductor crystals (OSCs) has led to significant theoretical findings and the development of innovative methods.

In studying the transport mechanism along 1D Pentacene (PEN) stacks, it has been confirmed that dynamic contributions play a crucial role. Specifically, the rotations of PEN linkers around the 6,13-axis result in fluctuations in inter-PEN electronic coupling and dynamic disorder. This dynamic behavior leads to partial hole delocalization and a unique charge transport mechanism that lies between localized hopping and delocalized transport. By conducting detailed quantum-mechanical investigations, a deeper understanding of the fundamental principles governing the charge carrier properties of OSC arrays has been achieved.

Additionally, a method to restrain specific eigenmodes while preserving the overall system dynamics has been successfully developed. The findings highlight the importance of mean hole coupling changes, along with fluctuations in hole couplings, in distinguishing killer modes. Removing certain eigenmodes significantly increases charge mobility and enhances molecular delocalization, attributed to reduced hole coupling fluctuations. The method's versatility allows for application to other oligoacene crystals without anthracene-specific components.

Moreover, a multiscale approach utilizing neural network models and the fewest switches surface hopping (FSSH) algorithm has been developed for simulating Frenkel singlet exciton propagation in OSCs. By accurately predicting site energies, excitonic couplings, and their derivatives, the method enables non-adiabatic molecular dynamics simulations. The long-range correction version of time-dependent density functional tight-binding with self-consistent charges (TD-LC-DFTB2) has been employed to generate high-quality data for training the neural networks. Exciton diffusion constants for various OSCs, including Anthrane (ANT), Pentacene (PEN), Perylenediimide

(PDI), and Diindenoperylene (DIP), have been calculated, yielding results in agreement with experimental values and other theoretical studies.

These findings contribute to a deeper understanding of charge and exciton transfer in OSCs and hold promise for future research. Expanding simulations to include other oligomers will provide a broader understanding of charge carrier behavior in different molecular systems. Additionally, further investigations into the impact of eigenmode constraints on charge mobility and the application of the developed method to other OSCs, such as pentacene, rubrene, and other relevant molecules, will enhance the robustness and applicability of the approach. Comparisons with existing literature analyses of charge transport and thermal disorder will validate the method and provide valuable insights for the design and optimization of organic electronic devices.

In conclusion, the investigation of charge and exciton transfer in OSCs has advanced our knowledge of their fundamental properties and behavior. The combination of theoretical analyses, computational simulations, and the development of innovative methods paves the way for future advancements in the field of organic electronics, enabling the design of efficient and optimized materials for various applications.

Bibliography

[1] Neal R Armstrong et al. "Organic/organic heterojunctions: organic light emitting diodes and organic photovoltaic devices". In: *Macromolecular rapid communications* 30.9-10 (2009), pp. 717–731.

[2] Rico Meerheim, BjÖrn Lussem, and Karl Leo. "Efficiency and stability of pin type organic light emitting diodes for display and lighting applications". In: *Proceedings of the IEEE* 97.9 (2009), pp. 1606–1626.

[3] Neal R Armstrong et al. "Organic/organic heterojunctions: organic light emitting diodes and organic photovoltaic devices". In: *Macromolecular rapid communications* 30.9-10 (2009), pp. 717–731.

[4] Carsten Deibel and Vladimir Dyakonov. "Polymer–fullerene bulk heterojunction solar cells". In: *Reports on Progress in Physics* 73.9 (2010), p. 096401.

[5] Gilles Dennler, Markus C Scharber, and Christoph J Brabec. "Polymer-fullerene bulk-heterojunction solar cells". In: *Advanced materials* 21.13 (2009), pp. 1323–1338.

[6] Carsten Deibel and Vladimir Dyakonov. "Polymer–fullerene bulk heterojunction solar cells". In: *Reports on Progress in Physics* 73.9 (2010), p. 096401.

[7] Christos D Dimitrakopoulos and Patrick RL Malenfant. "Organic thin film transistors for large area electronics". In: *Advanced materials* 14.2 (2002), pp. 99–117.

[8] Christopher R Newman et al. "Introduction to organic thin film transistors and design of n-channel organic semiconductors". In: *Chemistry of materials* 16.23 (2004), pp. 4436–4451.

[9] Antonio Facchetti. "Semiconductors for organic transistors". In: *materials today* 10.3 (2007), pp. 28–37.

[10] Anamika Dey et al. "Organic semiconductors: a new future of nanodevices and applications". In: *Thin Film Structures in Energy Applications* (2015), pp. 97–128.

[11] Ritesh Haldar et al. “Interplay of structural dynamics and electronic effects in an engineered assembly of pentacene in a metal–organic framework”. In: *Chemical science* 12.12 (2021), pp. 4477–4483.

[12] Weiwei Xie et al. “Performance of Mixed Quantum-Classical Approaches on Modeling the Crossover from Hopping to Bandlike Charge Transport in Organic Semiconductors”. In: *Journal of Chemical Theory and Computation* 16.4 (2020). PMID: 32176844, pp. 2071–2084. DOI: 10.1021/acs.jctc.9b01271.

[13] Samuele Giannini et al. “Exciton transport in molecular organic semiconductors boosted by transient quantum delocalization”. In: *Nature Communications* 13.1 (2022), p. 2755. DOI: 10.1038/s41467-022-30308-5. URL: https://doi.org/10.1038/s41467-022-30308-5.

[14] Sara Roosta et al. “Efficient surface hopping approach for modeling charge transport in organic semiconductors”. In: *Journal of Chemical Theory and Computation* 18.3 (2022), pp. 1264–1274.

[15] Alexander Heck et al. “Multi-Scale Approach to Non-Adiabatic Charge Transport in High-Mobility Organic Semiconductors”. In: *Journal of Chemical Theory and Computation* 11.11 (2015). PMID: 26574305, pp. 5068–5082. DOI: 10.1021/acs.jctc.5b00719.

[16] Jonas Lederer et al. “Machine learning–based charge transport computation for pentacene”. In: *Advanced Theory and Simulations* 2.2 (2019), p. 1800136.

[17] Onur Caylak, Anil Yaman, and Björn Baumeier. “Evolutionary approach to constructing a deep feedforward neural network for prediction of electronic coupling elements in molecular materials”. In: *Journal of chemical theory and computation* 15.3 (2019), pp. 1777–1784.

[18] Mila Krämer et al. “Charge and exciton transfer simulations using machine-learned Hamiltonians”. In: *Journal of chemical theory and computation* 16.7 (2020), pp. 4061–4070.

[19] Florian Häse et al. “Machine learning exciton dynamics”. In: *Chemical Science* 7.8 (2016), pp. 5139–5147.

[20] M. Elstner et al. “Self-consistent-charge density-functional tight-binding method for simulations of complex materials properties”. In: *Phys. Rev. B* 58 (11 Sept. 1998), pp. 7260–7268. DOI: 10.1103/PhysRevB.58.7260. URL: https://link.aps.org/doi/10.1103/PhysRevB.58.7260.

[21] Adam Kubas et al. “Electronic couplings for molecular charge transfer: Benchmarking CDFT, FODFT, and FODFTB against high-level ab initio calculations”. In: *The Journal of chemical physics* 140.10 (2014), p. 104105.

[22] Julian J. Kranz and Marcus Elstner. “Simulation of Singlet Exciton Diffusion in Bulk Organic Materials”. In: *Journal of Chemical Theory and Computation* 12.9 (2016). PMID: 27434173, pp. 4209–4221. DOI: 10.1021/acs.jctc.6b00235. eprint: https://doi.org/10.1021/acs.jctc.6b00235. URL: https://doi.org/10.1021/acs.jctc.6b00235.

[23] Beatrix M. Bold et al. “Benchmark and performance of long-range corrected time-dependent density functional tight binding (LC-TD-DFTB) on rhodopsins and light-harvesting complexes”. In: *Phys. Chem. Chem. Phys.* 22 (19 2020), pp. 10500–10518. DOI: 10.1039/C9CP05753F. URL: http://dx.doi.org/10.1039/C9CP05753F.

[24] Alexander Humeniuk and Roland Mitri. “Long-range correction for tight-binding TD-DFT”. In: *The Journal of Chemical Physics* 143.13 (2015), p. 134120. DOI: 10.1063/1.4931179. eprint: https://aip.scitation.org/doi/pdf/10.1063/1.4931179. URL: https://aip.scitation.org/doi/abs/10.1063/1.4931179.

[25] Monja Sokolov et al. “Analytical Time-Dependent Long-Range Corrected Density Functional Tight Binding (TD-LC-DFTB) Gradients in DFTB+: Implementation and Benchmark for Excited-State Geometries and Transition Energies”. In: *Journal of Chemical Theory and Computation* 17.4 (2021). PMID: 33689344, pp. 2266–2282. DOI: 10.1021/acs.jctc.1c00095. eprint: https://doi.org/10.1021/acs.jctc.1c00095. URL: https://doi.org/10.1021/acs.jctc.1c00095.

[26] Junmei Wang et al. “Development and testing of a general amber force field”. In: *Journal of computational chemistry* 25.9 (2004), pp. 1157–1174.

[27] Wolfgang Damm et al. “OPLS all-atom force field for carbohydrates”. In: *Journal of computational chemistry* 18.16 (1997), pp. 1955–1970.

[28] Tomáš Kubař and Marcus Elstner. “A hybrid approach to simulation of electron transfer in complex molecular systems”. In: *Journal of The Royal Society Interface* 10.87 (2013), p. 20130415. DOI: 10.1098/rsif.2013.0415.

[29] Enrico Tapavicza et al. “Ab initio non-adiabatic molecular dynamics”. In: *Physical Chemistry Chemical Physics* 15.42 (2013), pp. 18336–18348.

[30] J. Spencer, F. Gajdos, and J. Blumberger. "FOB-SH: Fragment orbital-based surface hopping for charge carrier transport in organic and biological molecules and materials". In: *The Journal of Chemical Physics* 145.6 (Aug. 2016). 064102. ISSN: 0021-9606. DOI: 10.1063/1.4960144. URL: https://doi.org/10.1063/1.4960144.

[31] Antoine Carof, Samuele Giannini, and Jochen Blumberger. "Detailed balance, internal consistency, and energy conservation in fragment orbital-based surface hopping". In: *The Journal of Chemical Physics* 147.21 (Dec. 2017). 214113. ISSN: 0021-9606. DOI: 10.1063/1.5003820. URL: https://doi.org/10.1063/1.5003820.

[32] Alexey V Akimov and Oleg V Prezhdo. "The PYXAID program for non-adiabatic molecular dynamics in condensed matter systems". In: *Journal of chemical theory and computation* 9.11 (2013), pp. 4959–4972.

[33] Harald Oberhofer, Karsten Reuter, and Jochen Blumberger. "Charge transport in molecular materials: An assessment of computational methods". In: *Chemical reviews* 117.15 (2017), pp. 10319–10357.

[34] Alessandro Troisi and David L. Cheung. "Transition from dynamic to static disorder in one-dimensional organic semiconductors". In: *The Journal of Chemical Physics* 131.1 (July 2009). 014703. ISSN: 0021-9606. DOI: 10.1063/1.3167406. URL: https://doi.org/10.1063/1.3167406.

[35] R. A. Marcus. "On the Theory of Oxidation-Reduction Reactions Involving Electron Transfer. I". In: *The Journal of Chemical Physics* 24.5 (Dec. 2004), pp. 966–978. ISSN: 0021-9606. DOI: 10.1063/1.1742723. URL: https://doi.org/10.1063/1.1742723.

[36] Vera Stehr et al. "Singlet exciton diffusion in organic crystals based on Marcus transfer rates". In: *Journal of Chemical Theory and Computation* 10.3 (2014), pp. 1242–1255.

[37] Adam Kubas et al. "Electronic couplings for molecular charge transfer: benchmarking CDFT, FODFT and FODFTB against high-level ab initio calculations. II". In: *Physical Chemistry Chemical Physics* 17.22 (2015), pp. 14342–14354.

[38] Alexander Heck et al. "Multi-scale approach to non-adiabatic charge transport in high-mobility organic semiconductors". In: *Journal of chemical theory and computation* 11.11 (2015), pp. 5068–5082.

[39] Balint Aradi, Ben Hourahine, and Th Frauenheim. "DFTB+, a sparse matrix-based implementation of the DFTB method". In: *The Journal of Physical Chemistry A* 111.26 (2007), pp. 5678–5684.

[40] Lucas Ueberricke et al. "Di-and Tetracyano-Substituted Pyrene-Fused Pyrazaacenes: Aggregation in the Solid State". In: *Chemistry–A European Journal* 26.50 (2020), pp. 11634–11642.

[41] Lucas Ueberricke et al. "Quinoxalinophenanthrophenazine Based Cruciforms". In: *European Journal of Organic Chemistry* 2021.34 (2021), pp. 4816–4823.

[42] Lucas Ueberricke et al. "Isostructural Charge-Transfer Cocrystals Based on Triptycene End-Capped Quinoxalinophenanthrophenazine". In: *Crystal Growth & Design* 21.2 (2021), pp. 1329–1341. DOI: 10.1021/acs.cgd.0c01619. URL: https://doi.org/10.1021/acs.cgd.0c01619.

[43] Lucas Ueberricke et al. "Triptycene End-Capped Benzothienobenzothiophene and Naphthothienobenzothiophene". In: *Chemistry–A European Journal* 26.55 (2020), pp. 12596–12605.

[44] Lisa Roß et al. "Two Dimensional Triptycene End-Capping and Its Influence on the Self-Assembly of Quinoxalinophenanthrophenazines". In: *Chinese Journal of Chemistry* ().

[45] Oleksandr V. Mikhnenko, Paul W. M. Blom, and Thuc-Quyen Nguyen. "Exciton diffusion in organic semiconductors". In: *Energy Environ. Sci.* 8 (7 2015), pp. 1867–1888. DOI: 10.1039/C5EE00925A.

[46] Tanguy Jousselin-Oba et al. "Excellent semiconductors based on tetracenotetracene and pentacenopentacene: From stable closed-shell to singlet open-shell". In: *Journal of the American Chemical Society* 141.23 (2019), pp. 9373–9381.

[47] Anthony J Petty et al. "Computationally aided design of a high-performance organic semiconductor: the development of a universal crystal engineering core". In: *Chemical Science* 10.45 (2019), pp. 10543–10549.

[48] Hakan Usta et al. "High electron mobility in [1] benzothieno [3, 2-b][1] benzothiophene-based field-effect transistors: toward n-type BTBTs". In: *Chemistry of Materials* 31.14 (2019), pp. 5254–5263.

[49] Kevin M Felter et al. "Interplay between charge carrier mobility, exciton diffusion, crystal packing, and charge separation in perylene diimide-based heterojunctions". In: *ACS Applied Energy Materials* 2.11 (2019), pp. 8010–8021.

[50] Takayoshi Kubo et al. “Suppressing molecular vibrations in organic semiconductors by inducing strain”. In: *Nature communications* 7.1 (2016), p. 11156.

[51] Masahiko Ando et al. “Disorder and localization dynamics in polymorphs of the molecular semiconductor pentacene probed by in situ micro-Raman spectroscopy and molecular dynamics simulations”. In: *Physical Review Materials* 3.2 (2019), p. 025601.

[52] Simone Fratini et al. “A map of high-mobility molecular semiconductors”. In: *Nature materials* 16.10 (2017), pp. 998–1002.

[53] Steffen Illig et al. “Reducing dynamic disorder in small-molecule organic semiconductors by suppressing large-amplitude thermal motions”. In: *Nature communications* 7.1 (2016), p. 10736.

[54] Kathryn A McGarry et al. “Rubrene-based single-crystal organic semiconductors: synthesis, electronic structure, and charge-transport properties”. In: *Chemistry of Materials* 25.11 (2013), pp. 2254–2263.

[55] Bolong Zhang et al. “Highly fluorescent molecularly insulated perylene diimides: Effect of concentration on photophysical properties”. In: *Chemistry of Materials* 29.19 (2017), pp. 8395–8403.

[56] Dylan H Arias et al. “Polymorphism influences singlet fission rates in tetracene thin films”. In: *Chemical Science* 7.2 (2016), pp. 1185–1191.

[57] Xiaopeng Wang et al. “Effect of crystal packing on the excitonic properties of rubrene polymorphs”. In: *CrystEngComm* 18.38 (2016), pp. 7353–7362.

[58] John E Anthony et al. “Functionalized pentacene: Improved electronic properties from control of solid-state order”. In: *Journal of the American Chemical Society* 123.38 (2001), pp. 9482–9483.

[59] John E Anthony, David L Eaton, and Sean R Parkin. “A road map to stable, soluble, easily crystallized pentacene derivatives”. In: *Organic letters* 4.1 (2002), pp. 15–18.

[60] Simon Lukas et al. “Epitaxial growth of pentacene films on metal surfaces”. In: *ChemPhysChem* 5.2 (2004), pp. 266–270.

[61] Susumu Kitagawa, Ryo Kitaura, and Shin-ichiro Noro. “Functional porous coordination polymers”. In: *Angewandte Chemie International Edition* 43.18 (2004), pp. 2334–2375.

[62] Hiroyasu Furukawa et al. “The chemistry and applications of metal-organic frameworks”. In: *Science* 341.6149 (2013), p. 1230444.

[63] Satoshi Horike, Satoru Shimomura, and Susumu Kitagawa. “Soft porous crystals”. In: *Nature chemistry* 1.9 (2009), pp. 695–704.

[64] Samuele Giannini et al. “Quantum localization and delocalization of charge carriers in organic semiconducting crystals”. In: *Nature Communications* 10.1 (2019), p. 3843.

[65] Asif Bashir et al. “Charge carrier mobilities in organic semiconductors: crystal engineering and the importance of molecular contacts”. In: *Physical Chemistry Chemical Physics* 17.34 (2015), pp. 21988–21996.

[66] Junmei Wang et al. “Development and testing of a general amber force field”. In: *Journal of Computational Chemistry* 25.9 (2004), pp. 1157–1174. DOI: https://doi.org/10.1002/jcc.20035. URL: https://onlinelibrary.wiley.com/doi/abs/10.1002/jcc.20035.

[67] Junmei Wang et al. “Automatic atom type and bond type perception in molecular mechanical calculations”. In: *Journal of Molecular Graphics and Modelling* 25.2 (2006), pp. 247–260. ISSN: 1093-3263. DOI: https://doi.org/10.1016/j.jmgm.2005.12.005. URL: https://www.sciencedirect.com/science/article/pii/S1093326305001737.

[68] U. Chandra Singh and Peter A. Kollman. “An approach to computing electrostatic charges for molecules”. In: *Journal of Computational Chemistry* 5.2 (1984), pp. 129–145. DOI: https://doi.org/10.1002/jcc.540050204. eprint: https://onlinelibrary.wiley.com/doi/pdf/10.1002/jcc.540050204. URL: https://onlinelibrary.wiley.com/doi/abs/10.1002/jcc.540050204.

[69] Brent H. Besler, Kenneth M. Merz Jr., and Peter A. Kollman. “Atomic charges derived from semi-empirical methods”. In: *Journal of Computational Chemistry* 11.4 (1990), pp. 431–439. DOI: https://doi.org/10.1002/jcc.540110404. eprint: https://onlinelibrary.wiley.com/doi/pdf/10.1002/jcc.540110404. URL: https://onlinelibrary.wiley.com/doi/abs/10.1002/jcc.540110404.

[70] G. A. Petersson et al. “A complete basis set model chemistry. I. The total energies of closed-shell atoms and hydrides of the first-row elements”. In: *The Journal of Chemical Physics* 89.4 (1988), pp. 2193–2218. DOI: 10.1063/1.455064. eprint: https://doi.org/10.1063/1.455064. URL: https://doi.org/10.1063/1.455064.

[71] G. A. Petersson and Mohammad A. Al-Laham. "A complete basis set model chemistry. II. Open-shell systems and the total energies of the first-row atoms". In: *The Journal of Chemical Physics* 94.9 (1991), pp. 6081–6090. DOI: 10.1063/1.460447. eprint: https://doi.org/10.1063/1.460447. URL: https://doi.org/10.1063/1.460447.

[72] M. J. Frisch et al. *Gaussian~16 Revision C.01.* Gaussian Inc. Wallingford CT. 2016.

[73] D. J. Evans and B. L. Holian. "The Nose–Hoover thermostat". In: *The Journal of Chemical Physics* 83.8 (1985), pp. 4069–4074. DOI: 10.1063/1.449071. eprint: https://doi.org/10.1063/1.449071. URL: https://doi.org/10.1063/1.449071.

[74] Alessandro Troisi and Giorgio Orlandi. "Dynamics of the intermolecular transfer integral in crystalline organic semiconductors". In: *The Journal of Physical Chemistry A* 110.11 (2006), pp. 4065–4070.

[75] Alessandro Troisi. "Prediction of the absolute charge mobility of molecular semiconductors: the case of rubrene". In: *Advanced Materials* 19.15 (2007), pp. 2000–2004.

[76] Guillaume Schweicher et al. "Chasing the "killer" phonon mode for the rational design of low-disorder, high-mobility molecular semiconductors". In: *Advanced Materials* 31.43 (2019), p. 1902407.

[77] Mark J. Abraham et al. "GROMACS: High performance molecular simulations through multi-level parallelism from laptops to supercomputers". In: *SoftwareX* 1-2 (2015), pp. 19–25. DOI: 10.1016/j.softx.2015.06.001.

[78] Gareth A. Tribello et al. "PLUMED 2: New feathers for an old bird". In: *Computer Physics Communications* 185.2 (2014), pp. 604–613. DOI: 10.1016/j.cpc.2013.09.018.

[79] Frank C. Spano. "The Spectral Signatures of Frenkel Polarons in H- and J-Aggregates". In: *Accounts of Chemical Research* 43.3 (2010). PMID: 20014774, pp. 429–439. DOI: 10.1021/ar900233v. eprint: https://doi.org/10.1021/ar900233v. URL: https://doi.org/10.1021/ar900233v.

[80] V V Egorov and M V Alfimov. "Theory of the J-band: from the Frenkel exciton to charge transfer". In: *Physics-Uspekhi* 50.10 (Oct. 2007), p. 985. DOI: 10.1070/PU2007v050n10ABEH006317. URL: https://dx.doi.org/10.1070/PU2007v050n10ABEH006317.

[81] Henk Fidder, Jacob Terpstra, and Douwe A. Wiersma. "Dynamics of Frenkel excitons in disordered molecular aggregates". In: *The Journal of Chemical Physics* 94.10 (1991), pp. 6895–6907. DOI: 10.1063/1.460220. eprint: https://doi.org/10.1063/1.460220. URL: https://doi.org/10.1063/1.460220.

[82] Per-Arno Plötz, Thomas Niehaus, and Oliver Kühn. "A new efficient method for calculation of Frenkel exciton parameters in molecular aggregates". In: *The Journal of Chemical Physics* 140.17 (2014), p. 174101. DOI: 10.1063/1.4871658. eprint: https://doi.org/10.1063/1.4871658. URL: https://doi.org/10.1063/1.4871658.

[83] M. Elstner et al. "Self-consistent-charge density-functional tight-binding method for simulations of complex materials properties". In: *Phys. Rev. B* 58 (11 Sept. 1998), pp. 7260–7268. DOI: 10.1103/PhysRevB.58.7260. URL: https://link.aps.org/doi/10.1103/PhysRevB.58.7260.

[84] Juan Aragó and Alessandro Troisi. "Excitonic couplings between molecular crystal pairs by a multistate approximation". In: *The Journal of Chemical Physics* 142.16 (2015), p. 164107. DOI: 10.1063/1.4919241. eprint: https://doi.org/10.1063/1.4919241. URL: https://doi.org/10.1063/1.4919241.

[85] Kurt A. Kistler, Francis C. Spano, and Spiridoula Matsika. "A Benchmark of Excitonic Couplings Derived from Atomic Transition Charges". In: *The Journal of Physical Chemistry B* 117.7 (2013). PMID: 23391106, pp. 2032–2044. DOI: 10.1021/jp310603z. eprint: https://doi.org/10.1021/jp310603z. URL: https://doi.org/10.1021/jp310603z.

[86] J.C. Gower and G.B. Dijksterhuis. *Procrustes Problems*. Oxford Statistical Science Series. OUP Oxford, 2004. ISBN: 9780191545337. URL: https://books.google.de/books?id=kRRREAAAQBAJ.

[87] BP Flannery et al. *Numerical recipes 3rd edition: The art of scientific computing*. Cambridge university press, 2007.

[88] Jonas Lederer et al. "Machine learning–based charge transport computation for pentacene". In: *Advanced Theory and Simulations* 2.2 (2019), p. 1800136.

[89] Félix Musil et al. "Machine learning for the structure–energy–property landscapes of molecular crystals". In: *Chemical science* 9.5 (2018), pp. 1289–1300.

[90] Jingbai Li et al. “Automatic discovery of photoisomerization mechanisms with nanosecond machine learning photodynamics simulations”. In: *Chemical science* 12.14 (2021), pp. 5302–5314.

[91] Julian J Kranz and Marcus Elstner. “Simulation of singlet exciton diffusion in bulk organic materials”. In: *Journal of chemical theory and computation* 12.9 (2016), pp. 4209–4221.

[92] Juan Aragó et al. “Ab Initio Modeling of Donor–Acceptor Interactions and Charge-Transfer Excitations in Molecular Complexes: The Case of Terthiophene–Tetracyanoquinodimethane”. In: *Journal of Chemical Theory and Computation* 7.7 (2011). PMID: 26606478, pp. 2068–2077. DOI: 10.1021/ct200203k. eprint: https://doi.org/10.1021/ct200203k. URL: https://doi.org/10.1021/ct200203k.

[93] Lisha Li et al. “Hyperband: A novel bandit-based approach to hyperparameter optimization”. In: *The Journal of Machine Learning Research* 18.1 (2017), pp. 6765–6816.

A. Appendix

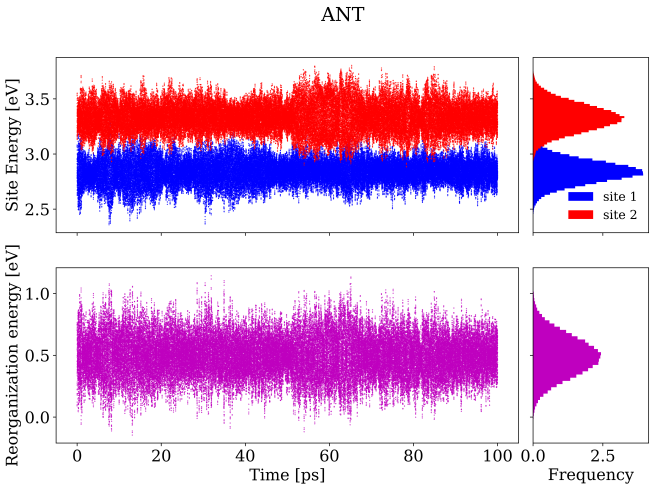

Figure A.1.: ANT site energies and reorganization energy distributions, predicted by NN during the NAMD simulation

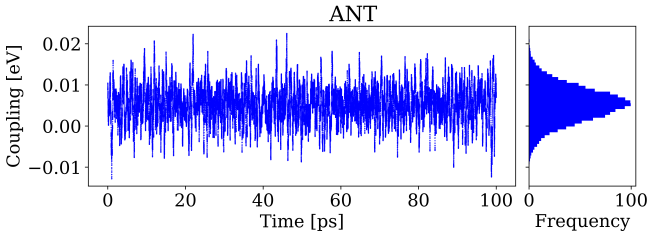

Figure A.2.: ANT adir TrMull coupling distribution, predicted by NN during the NAMD simulation

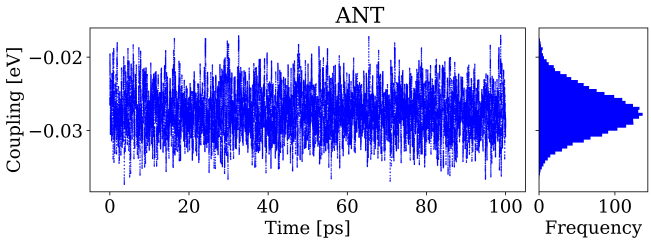

Figure A.3.: ANT bdir TrMull coupling distribution, predicted by NN during the NAMD simulation

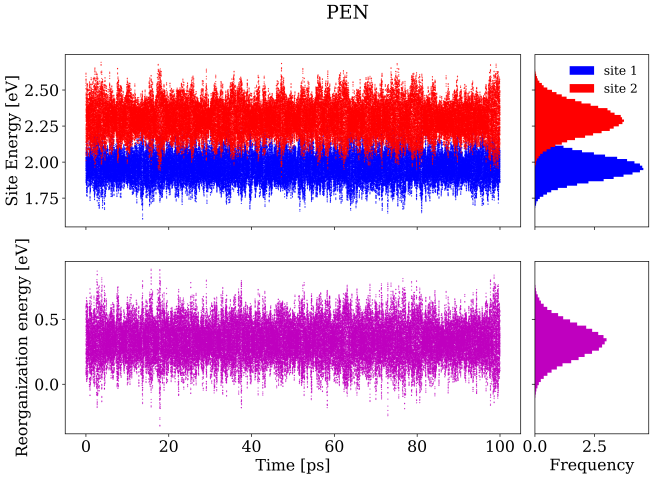

Figure A.4.: PEN site energies and reorganization energy distributions, predicted by NN during the NAMD simulation

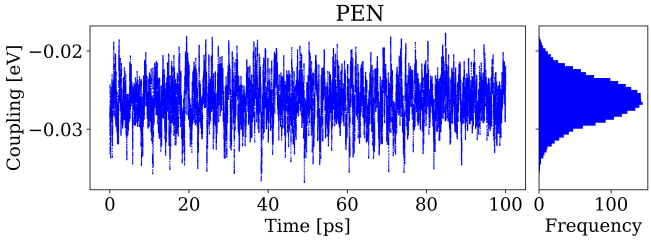

Figure A.5.: PEN pdir TrMull coupling distribution, predicted by NN during the NAMD simulation

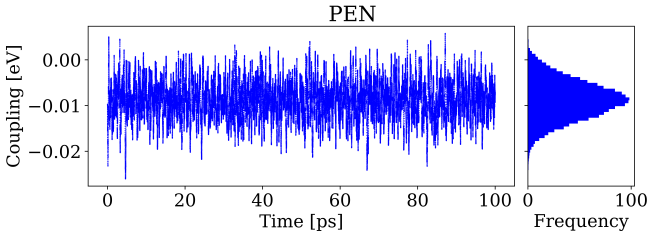

Figure A.6.: PEN t1dir TrMull coupling distribution, predicted by NN during the NAMD simulation

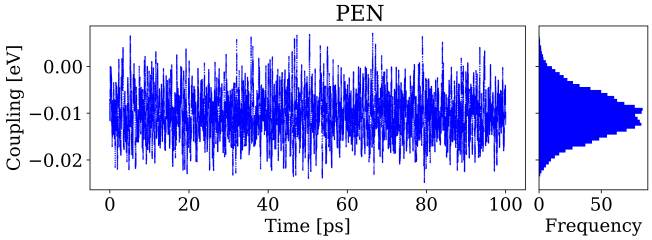

Figure A.7.: PEN t2dir TrMull coupling distribution, predicted by NN during the NAMD simulation

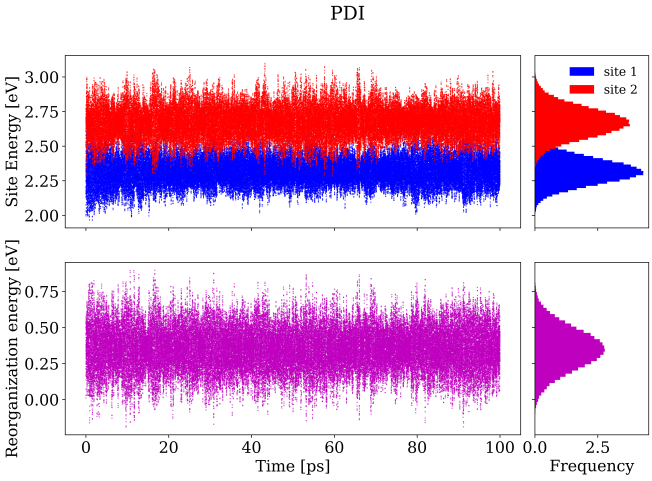

Figure A.8.: PDI site energies and reorganization energy distributions, predicted by NN during the NAMD simulation

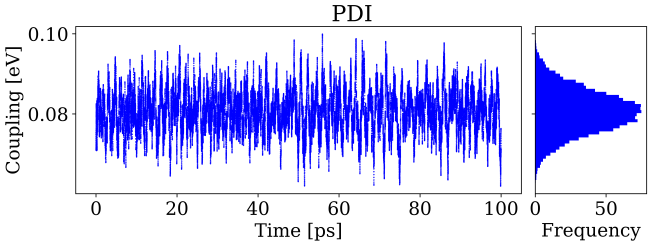

Figure A.9.: PDI pdir TrMull coupling distribution, predicted by NN during the NAMD simulation

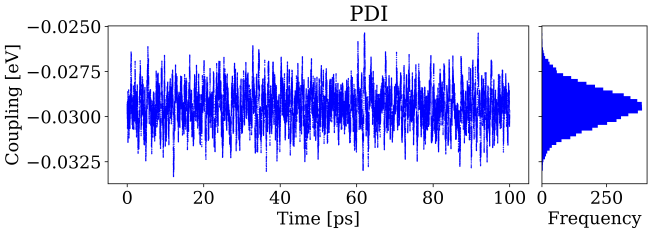

Figure A.10.: PDI t1dir TrMull coupling distribution, predicted by NN during the NAMD simulation

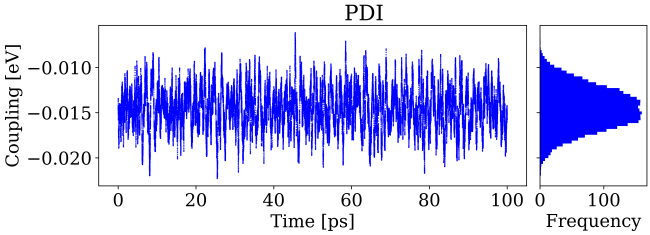

Figure A.11.: PDI t2dir TrMull coupling distribution, predicted by NN during the NAMD simulation

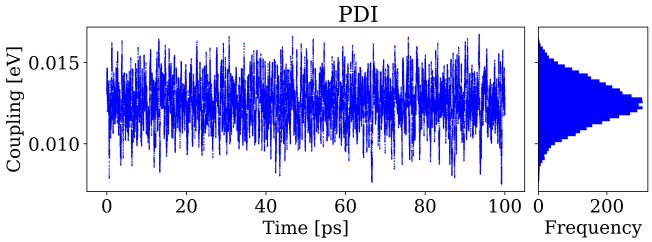

Figure A.12.: PDI t3dir TrMull coupling distribution, predicted by NN during the NAMD simulation

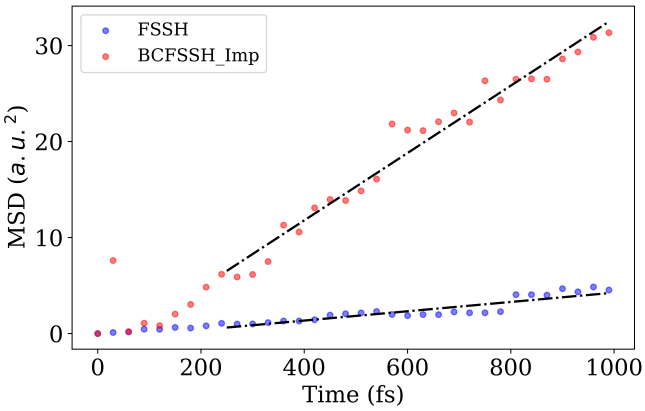

Figure A.13.: ANT MSD adir calculated from NAMD simulation

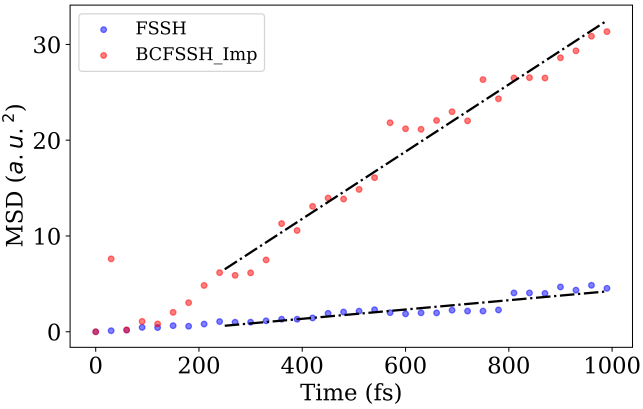

Figure A.14.: ANT MSD bdir calculated from NAMD simulation

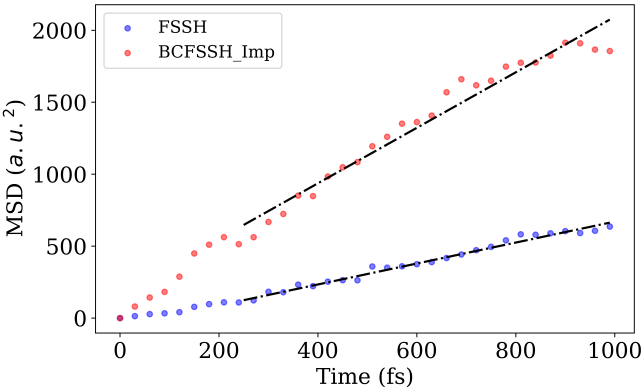

Figure A.15.: PEN MSD pdir calculated from NAMD simulation

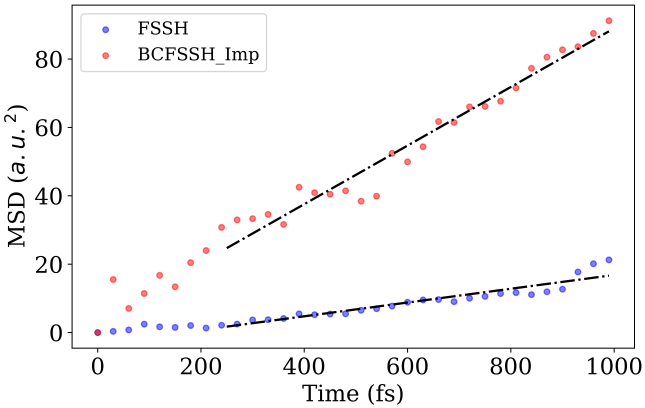

Figure A.16.: PEN MSD t1dir calculated from NAMD simulation

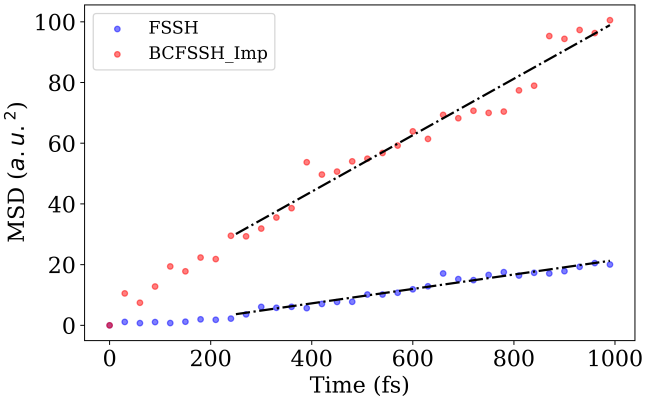

Figure A.17.: PEN MSD t2dir calculated from NAMD simulation

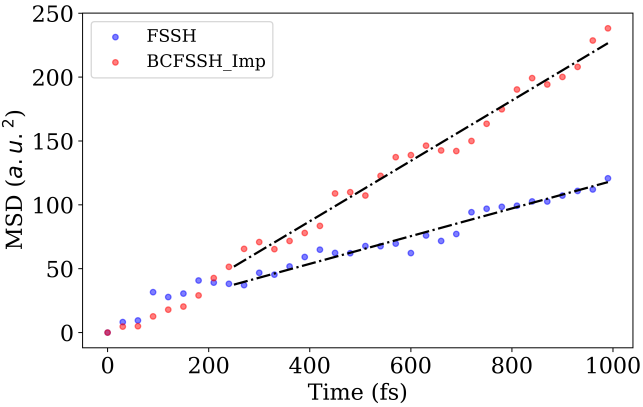

Figure A.18.: PDI MSD t1dir calculated from NAMD simulation